

On non-Oberbeck-Boussinesq effects in three-dimensional Rayleigh-Bénard convection in glycerol

Horn, S., Shishkina, O. & Wagner, C.

Author post-print (accepted) deposited by Coventry University's Repository

Original citation & hyperlink:

[Horn, S, Shishkina, O & Wagner, C 2013, 'On non-Oberbeck-Boussinesq effects in three-dimensional Rayleigh-Bénard convection in glycerol' Journal of Fluid Mechanics, vol. 724, pp. 175-202.

<https://dx.doi.org/10.1017/jfm.2013.151>

DOI 10.1017/jfm.2013.151

ISSN 0022-1120

ESSN 1469-7645

Publisher: Cambridge University Press

Copyright © and Moral Rights are retained by the author(s) and/ or other copyright owners. A copy can be downloaded for personal non-commercial research or study, without prior permission or charge. This item cannot be reproduced or quoted extensively from without first obtaining permission in writing from the copyright holder(s). The content must not be changed in any way or sold commercially in any format or medium without the formal permission of the copyright holders.

This document is the author's post-print version, incorporating any revisions agreed during the peer-review process. Some differences between the published version and this version may remain and you are advised to consult the published version if you wish to cite from it.

On non-Oberbeck–Boussinesq effects in three-dimensional Rayleigh–Bénard convection in glycerol

SUSANNE HORN, OLGA SHISHKINA
AND CLAUS WAGNER

Institute of Aerodynamics and Flow Technology, German Aerospace Center (DLR),
Bunsenstr a e 10, 37073 G ottingen, Germany

(Received ?; revised ?; accepted ?. - To be entered by editorial office)

Rayleigh–B enard convection in glycerol (Prandtl number $Pr = 2547.9$) in a cylindrical cell with an aspect ratio of $\Gamma = 1$ was studied by means of three-dimensional direct numerical simulations (DNS). For that purpose, we implemented temperature-dependent material properties into our DNS code, by prescribing polynomial functions up to seventh order for the viscosity, the heat conductivity and the density. We performed simulations with the common Oberbeck–Boussinesq (OB) approximation and with non-Oberbeck–Boussinesq (NOB) effects within a range of Rayleigh numbers of $10^5 \leq Ra \leq 10^9$. For the highest temperature differences, $\Delta = 80$ K, the viscosity at the top is about 360% times higher than at the bottom, while the differences of the other material properties are less than 15%. We analysed the temperature and velocity profiles and the thermal and viscous boundary layer thicknesses. NOB effects generally lead to a breakdown of the top–bottom symmetry, typical for OB Rayleigh–B enard convection. Under NOB conditions, the temperature in the centre of the cell T_c increases with increasing Δ and can be up to 15 K higher than under OB conditions. The comparison of our findings with several theoretical and empirical models showed that 2D boundary layer models overestimate the actual T_c , while models based on the temperature or velocity scales predict T_c very well with a standard deviation of 0.4 K. Furthermore, the obtained temperature profiles bend closer towards the cold top plate and further away from the hot bottom plate. The situation for the velocity profiles is reversed: they bend farther away from the top plate and closer towards to the bottom plate. The top boundary layers are always thicker than the bottom ones. Their ratio is up to 2.5 for the thermal and up to 4.5 for the viscous boundary layers. Additionally, the Reynolds number Re and the Nusselt number Nu were investigated: Re is higher and Nu is lower under NOB conditions. The Nusselt number Nu is influenced in a non-linear way by NOB effects, stronger than was suggested by the 2D simulations. The actual scaling of Nu with Ra in the NOB case is $Nu \propto Ra^{0.298}$ and is in excellent agreement with the experimental data.

Key Words:

1. Introduction

Understanding Rayleigh–B enard convection, i.e., a fluid heated from below and cooled from above, is a topic of ongoing interest in fluid dynamics. Trying to understand the particular case of Rayleigh–B enard convection in glycerol means facing two challenges at the same time. First of all, the standard approach of using the Oberbeck–Boussinesq (OB)

approximation (Boussinesq 1903; Oberbeck 1879) is not appropriate here, and second, glycerol has a very high but finite Prandtl number of $Pr = 2547.9$. Thus the inertial forces are small but not negligible, while the momentum is very diffusive.

The OB approximation is a well-established method for studying the idealised problem of Rayleigh–Bénard convection from a mathematical and numerical point of view. It assumes that all material properties are constant, in particular also the density. Correspondingly, the fluid is incompressible. However, within the buoyancy term, the density varies linearly with temperature. This might indeed be admissible in certain cases, but nonetheless, the range of validity of this approach is actually quite restricted. A rigorous deduction was given by Gray & Giorgini (1976) and the method will be briefly summarised in section 2. Deviations due to the violation of the OB assumption are commonly referred to as non-Oberbeck–Boussinesq (NOB) effects.

NOB effects have been studied theoretically by Busse (1967) in a Rayleigh number range close to the onset of convection. For higher Rayleigh numbers, and in particular in the turbulent regime, experiments have been conducted with gases at low temperature or close to the critical point, for example, in helium by Wu & Libchaber (1991), in ethane by Ahlers *et al.* (2007), and in sulfur hexa-fluoride by Burnishev *et al.* (2010). There the compressibility and the pressure dependence of the material properties play the most important role for NOB effects.

On the other hand, NOB effects in liquids almost solely originate from the temperature dependence of the material properties. And that is what we are going to focus on. As the starting point of our investigations we use the work by Ahlers *et al.* (2006). They have not only conducted experiments in water, but also made some hypothetical predictions for glycerol. Later, their research was complemented by 2D simulations in water and glycerol by Sugiyama *et al.* (2007, 2009).

However, the reliability of two-dimensional simulations to predict three-dimensional properties is debatable. Schmalzl *et al.* (2004) have investigated the difference between two- and three-dimensional simulations for a moderate Rayleigh number of $Ra = 10^6$ and $Pr \in [0.001, 100]$. They found that, e.g., the discrepancy in the Nusselt number Nu and the maximal horizontal root mean square (rms) velocity is about 80% for $Pr = 0.025$. In comparison to that, the calculations for $Pr = 100$ seemed to yield similar results in the two- and three-dimensional simulations. Nonetheless, the deviation in the Nusselt numbers and the maximal horizontal rms velocity was larger than 20%.

Glycerol has also been experimentally investigated by Zhang *et al.* (1997, 1998), but their experiments were conducted for a large range of Prandtl numbers ($600 \lesssim Pr \lesssim 8000$), a major shortcoming induced by the strongly varying viscosity. However, to draw quantitative conclusions, it is preferable to have a constant Pr . This can be achieved by means of numerical simulations, despite the fact that treating high Prandtl number fluids is very challenging due to the required mesh resolution, which will be corroborated in section 3.

As indicated above, thermal convection at large Pr exhibits very different characteristics compared to low and moderate Pr , even without NOB effects. But not much work has been devoted to this. A recent example to mention here is the work by Silano *et al.* (2010). They performed numerical simulations for $Pr = 1000$ and $Pr = 10000$ for up to $Ra = 10^9$ and up to $Ra = 10^7$, respectively. However, for $Ra = 10^9$ their computational mesh is very unlikely to be sufficiently fine to resolve the smallest scales, as is demanded by direct numerical simulations (DNS), cf. Shishkina *et al.* (2010); Stevens *et al.* (2010) and section 3.3. Generally, instead of conducting simulations at high Pr , rather the limit as Pr goes to infinity has been used, as, for example, by Busse (1979) and Constantin & Doering (1999) under OB conditions and Christensen & Harder (1991); Ogawa *et al.*

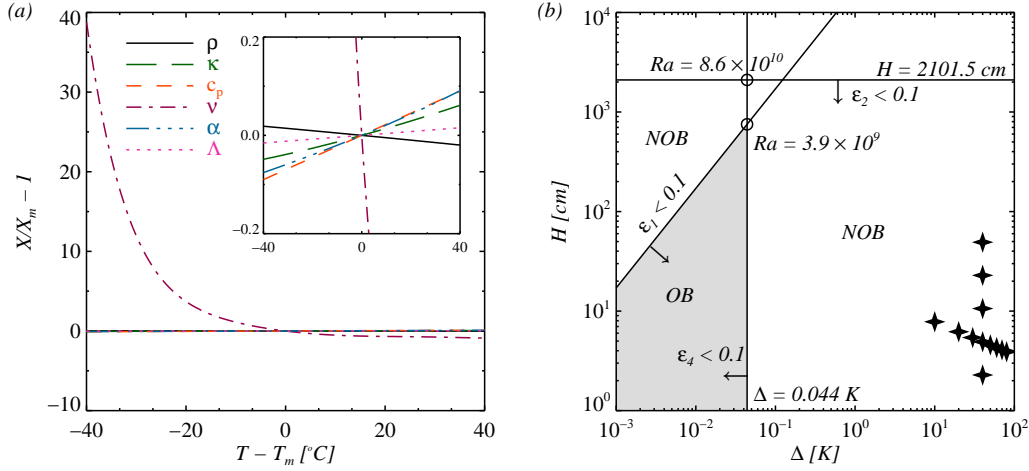


FIGURE 1. (a) Relative deviations of glycerol properties X from their values X_m at a mean temperature of $T_m = 40^\circ$, according to Segur & Oberstar (1951) and Ahlers *et al.* (2006); black solid line: density ρ ; green dashed line: thermal diffusivity κ ; orange short dashed line: specific heat capacity c_p ; purple dashed dotted line: kinematic viscosity ν ; blue dashed triple-dotted line: expansion coefficient α ; pink dotted line: thermal conductivity Λ . (b) Region of validity of the Oberbeck–Boussinesq approximation for glycerol at $T_m = 40^\circ\text{C}$, according to Gray & Giorgini (1976). The grey shaded area shows the parameter range where OB is applicable and our NOB DNS data points are denoted by stars. The restricting borders in terms of the ε_i factors are shown as well.

(1991) and Manga & Weeraratne (1999) with a temperature-dependent viscosity. While making analytical and numerical considerations simpler, this approach completely neglects effects induced by inertia.

Thus, the objective of this paper is twofold: First, to provide an accurate and extensive set of data for a high Pr fluid under strict OB conditions – which is only possible by means of well-resolved three-dimensional DNS, because experiments are unavoidably spoiled by NOB effects at higher Ra (cf. e.g. Xia *et al.* 2002). Second, to also evaluate the influence of NOB effects for that case.

2. Validity range of the OB approximation in the case of glycerol

The viscosity of glycerol is highly varying with temperature, as can be seen in figure 1 (a). Thus, it is already evident that glycerol cannot be described properly within the framework of the common OB approximation if the temperature difference Δ between the upper and lower plate becomes too large.

Gray & Giorgini (1976) provided a mathematically straightforward way to explicitly calculate the validity range of the OB approximation. Their final result is a requirement on certain ε_i factors to be smaller than a requested accuracy. Since we are only interested in NOB effects induced by the temperature dependence of the material properties, these are given by

$$\varepsilon_1 = \frac{\alpha_m g H T_m}{c_{p,m} \Delta}, \quad \varepsilon_2 = \frac{\alpha_m g H \nu_m}{c_{p,m} \kappa_m}, \quad \varepsilon_3 = -\frac{\Delta}{\rho_m} \frac{\partial \rho}{\partial T} \Big|_{T_m}, \quad \varepsilon_4 = \frac{\Delta}{c_{p,m}} \frac{\partial c_p}{\partial T} \Big|_{T_m},$$

$$\varepsilon_5 = \frac{\Delta}{\rho_m \nu_m} \frac{\partial(\rho\nu)}{\partial T} \Big|_{T_m}, \quad \varepsilon_6 = \frac{\Delta}{\Lambda_m} \frac{\partial \Lambda}{\partial T} \Big|_{T_m}, \quad \varepsilon_7 = \frac{\Delta}{\alpha_m} \frac{\partial \alpha}{\partial T} \Big|_{T_m}.$$

Here, T is the temperature, H the height of the Rayleigh–Bénard cell, g the acceleration due to gravity, α the isobaric expansion coefficient, ρ the density, ν the kinematic viscosity, Λ the heat conductivity, c_p the specific heat at constant pressure, and $\Delta = T_b - T_t$ the imposed adverse temperature difference. The indices t , b , and m here and in the following refer to the quantity at the top, the bottom, and the arithmetic mean temperature $T_m = (T_t + T_b)/2$, respectively. That means, that if $|\varepsilon_1| \dots |\varepsilon_7| \leq 0.1$, a residual error of at most 10% is guaranteed. The factor ε_3 represents the common $\alpha\Delta \leq 0.1$ criterion which is often quoted as being a sufficient criterion. An accurate calculation yields that the factors ε_1 and ε_4 for glycerol are the decisive parameters, requiring $H/\Delta < 170.986 \text{ mK}^{-1}$ and $\Delta < 0.04 \text{ K}$, respectively. The range of validity is also shown in figure 1 (b), along with the parameters of our performed NOB DNS.

Note that the Gray–Giorgini ansatz does not provide a criterion for a strong development of non-Oberbeck–Boussinesqness, which becomes visible already in such integral quantities like the Nusselt number or the centre temperature. As it was shown by Ahlers *et al.* (2006) and Sugiyama *et al.* (2007), these global parameters are affected mainly by higher order terms in the temperature dependences of the material parameters.

3. Numerical methodology

3.1. The basic Oberbeck–Boussinesq code

For our studies of OB Rayleigh–Bénard convection we perform DNS with a well-tested fourth order accurate finite volume code for cylindrical domains.

The code is based on `flowsi`, a DNS code for turbulent flow problems originally developed by Schmitt & Friedrich (1988). It solves the Navier–Stokes equations on staggered grids and uses the volume balance procedure motivated by Schumann (1975). Later on, it was advanced with a fourth order accurate spatial integration scheme and for the simulation of Rayleigh–Bénard convection by Shishkina & Wagner (2005, 2007b). As time integration scheme, a hybrid explicit/semi-implicit Euler–Leapfrog method is employed; a semi-implicit scheme close to the cylinder axis; and an explicit one elsewhere. For further details of the code’s current OB version, we also refer to Shishkina & Wagner (2007a).

3.2. Implementation of temperature-dependent material properties and governing equations

For the purpose of investigating NOB effects, we implemented temperature-dependent material properties (Horn *et al.* 2011) and applied it to the special case of glycerol. That is, the viscosity ν , the thermal conductivity Λ , the thermal diffusivity κ , and the density in the buoyancy term ρ are described by polynomials up to seventh order ($i = 7$),

$$\frac{X - X_m}{X_m} = \sum_i a_i (T - T_m)^i, \quad X = \nu, \Lambda, \kappa, \rho, \quad (3.1)$$

while the density ρ , except within the buoyancy term, and the isobaric specific heat capacity c_p are set constant to their values at the mean temperature T_m . The coefficients a_i for κ , α , and Λ are adopted from Ahlers *et al.* (2006), but their given polynomial for ν was not sufficient, since it led to negative viscosities for $T \gtrsim 70^\circ\text{C}$. Thus, we performed a least squares polynomial fit on the data from Segur & Oberstar (1951) ranging from 0°C to 100°C , leading to a mean viscosity of $\nu_m = 238.738 \times 10^{-6} \text{ m}^2 \text{ s}^{-1}$ and the following

coefficients:

$$\begin{aligned}
 a_1 &= -771.27 \times 10^{-10} \text{ K}^{-1} \text{ m}^2 \text{ s}^{-1}, & a_2 &= 2746.4 \times 10^{-12} \text{ K}^{-2} \text{ m}^2 \text{ s}^{-1}, \\
 a_3 &= -3257.1 \times 10^{-14} \text{ K}^{-3} \text{ m}^2 \text{ s}^{-1}, & a_4 &= 1513.2 \times 10^{-15} \text{ K}^{-4} \text{ m}^2 \text{ s}^{-1}, \\
 a_5 &= -1135.0 \times 10^{-16} \text{ K}^{-5} \text{ m}^2 \text{ s}^{-1}, & a_6 &= 261.07 \times 10^{-17} \text{ K}^{-6} \text{ m}^2 \text{ s}^{-1}, \\
 a_7 &= -18.682 \times 10^{-18} \text{ K}^{-7} \text{ m}^2 \text{ s}^{-1}.
 \end{aligned} \tag{3.2}$$

The approach described here is appropriate for most liquids, including glycerol, and accounts for the major relevant NOB effects.

The flow characteristics are obtained by solving the continuity equation (3.3), the Navier–Stokes equations (3.4), and the energy equation (3.5) for incompressible fluids in cylindrical coordinates (r, ϕ, z) , including the aforementioned material functions:

$$\frac{1}{r} \partial_r (r u_r) + \frac{1}{r} \partial_\phi u_\phi + \partial_z u_z = 0, \tag{3.3}$$

$$\begin{aligned}
 D_t u_r - \frac{u_\phi^2}{r} + \frac{1}{\rho_m} \partial_r p &= \frac{1}{r} \partial_r (r \nu \tilde{\tau}_{rr}) + \frac{1}{r} \partial_\phi (\nu \tilde{\tau}_{r\phi}) + \partial_z (\nu \tilde{\tau}_{rz}) - \frac{1}{r} \nu \tilde{\tau}_{\phi\phi}, \\
 D_t u_\phi + \frac{u_r u_\phi}{r} + \frac{1}{\rho_m} \frac{1}{r} \partial_\phi p &= \frac{1}{r^2} \partial_r (r^2 \nu \tilde{\tau}_{\phi r}) + \frac{1}{r} \partial_\phi (\nu \tilde{\tau}_{\phi\phi}) + \partial_z (\nu \tilde{\tau}_{\phi z}),
 \end{aligned} \tag{3.4}$$

$$\begin{aligned}
 D_t u_z + \frac{1}{\rho_m} \partial_z p &= \frac{1}{r} \partial_r (r \nu \tilde{\tau}_{zr}) + \frac{1}{r} \partial_\phi (\nu \tilde{\tau}_{z\phi}) + \partial_z (\nu \tilde{\tau}_{zz}) + \frac{\rho_m - \rho}{\rho_m} g, \\
 \rho_m c_{p,m} D_t T &= \frac{1}{r} \partial_r (\Lambda r \partial_r T) + \frac{1}{r^2} \partial_\phi (\Lambda \partial_\phi T) + \partial_z (\Lambda \partial_z T).
 \end{aligned} \tag{3.5}$$

Here, D_t denotes the substantial derivative, p the pressure, and u_r , u_ϕ , and u_z the radial, azimuthal, and vertical velocity component, respectively. The tensor $\tilde{\tau}$ is defined via the deviatoric stress tensor τ by $\tilde{\tau} = \tau / (\rho_m \nu)$. All other variables have their usual meaning and were already introduced in the previous section.

Non-dimensional equations, solved numerically, are obtained by using the physical parameters the radius R , the buoyancy velocity $\sqrt{g \alpha_m R \Delta}$, the temperature difference Δ , and the various material properties at the mean temperature, i.e. ν_m , Λ_m , ρ_m , as reference scales. In line with this, the reference time is given by $R / \sqrt{g \alpha_m R \Delta}$ and the reference pressure is $\rho_m g \alpha_m R \Delta$. The control parameters for our simulations are essentially the Rayleigh and the Prandtl number defined at the mean temperature T_m ,

$$Ra = Ra_m = \frac{\alpha_m g \Delta H^3}{\kappa_m \nu_m}, \quad Pr = Pr_m = \frac{\nu_m}{\kappa_m}. \tag{3.6}$$

For the time being, we restrict ourselves to cylindrical Rayleigh–Bénard cells with an aspect ratio of $\Gamma = 2R/H = 1$. We also introduce an alternative aspect ratio $\gamma = R/H = 0.5$ for later convenience.

As boundary conditions for the temperature, we impose adiabaticity of the lateral wall, and the top and bottom plate being isothermal, i.e., they have a constant dimensionless temperature $\hat{T}_t = -0.5$ and $\hat{T}_b = 0.5$, respectively. The hat indicates dimensionless quantities, but will be dropped for clarity in the following. As boundary conditions for the velocity, we apply impermeability and no-slip conditions at the walls. All boundary conditions are completed by setting a periodicity of 2π in the ϕ -direction.

3.3. Resolution

The high Prandtl number ($Pr = 2547.9$) puts severe constraints on the temporal and spatial resolution, making glycerol very challenging from a numerical point of view.

First of all, the instabilities due to momentum diffusion are damped much faster than

the instabilities in the temperature, and the system reacts almost instantaneously to temperature fluctuations. Thus, the temperature scales are much smaller than the velocity ones. As a result, the time to reach equilibrium and to gain reliable statistics is at least one order of magnitude longer, i.e., several thousand dimensionless time units.

Second, the system is known to be dominated by single plumes, also in the centre of the cell, which then occasionally cross the whole cell, as shown in figure 2. They also become thinner with increasing Ra , requiring a sufficient resolution not only in the boundary layers (BLs) but also within the bulk. Furthermore, the viscous boundary layer becomes much thicker than the thermal one and eventually saturates at a certain value (Grossmann & Lohse 2001; Breuer *et al.* 2004; Schmalzl *et al.* 2004). This cannot be described within the theory of mesh requirements proposed by Shishkina *et al.* (2010). We decided to take the criterion from Shishkina *et al.* (2010) for the mesh size in the Prandtl–Blasius type boundary layer and apply it to the whole domain and, moreover, we divided the required mesh size by a safety factor of 2 to consider NOB effects, i.e., all cells are smaller than

$$h^{BL} = \frac{1}{2} \left[2^{-3/2} a^{-1} E^{-3/2} Nu^{-3/2} H \right] \quad (a \approx 0.482, E \approx 0.982). \quad (3.7)$$

An estimation of the constants a and E can be found in Shishkina *et al.* (2010); the Nusselt number Nu , however, is an output parameter and we have to estimate it. We refrained from using the experimental data by Zhang *et al.* (1997) because all of their measurements were made for strongly varying Prandtl numbers and only for a range between 8.2×10^6 and 6.1×10^8 . Instead, we used the scaling laws suggested by Grossmann & Lohse (2000, 2001, 2002) as the best available estimate of the value of the Nusselt number. Remarkably, our glycerol simulations cross three regimes within a comparatively small range of Rayleigh numbers: I_∞ , I_u , and III_u (see table 1). Thus while for lower Rayleigh numbers the infinite Prandtl number assumption is a valid approximation, this becomes less true with increasing Ra . The Nusselt number calculated using the Grossmann–Lohse theory Nu_{GL} , the herewith a priori requested resolution h^{BL}/H , and the number of nodes in the radial, azimuthal, and vertical direction, are given in table 1. In addition we also show the actual maximal grid size in the boundary layers h/H , as well as the Nusselt number obtained in our OB simulations Nu_{OB}^{DNS} . Further details regarding the heat flux, including but not limited to the Nusselt number and its scaling, are discussed in section 4.7. Because of the very fine meshes we were allowed to distribute our nodes equidistantly and made use of this for $Ra = 10^7$, 10^8 and 10^9 . For smaller Ra , we used non-equidistant meshes where the nodes were clustered in the vicinity of the walls.

For $Ra = 10^9$, the maximal mesh size in the boundary layers is slightly smaller. However, a grid resolution study for the $Ra = 10^9$ simulation was also conducted, and revealed that the Nu_{DNS} obtained agrees well with the one obtained on a coarser grid with $192 \times 512 \times 384$ nodes (see table 1). We also verified our grid resolution with an a posteriori analysis, i.e., that the vertical grid spacing h_z is everywhere smaller than the smallest relevant length scale, the (non-dimensional) Batchelor length

$$\eta_B = \gamma^{-9/8} Pr^{-1/8} Ra^{-3/8} \epsilon_u^{-1/4}, \quad (3.8)$$

with the dimensionless kinetic energy dissipation rate

$$\epsilon_u = \gamma^{-3/2} Pr^{1/2} Ra^{-1/2} |\nabla \mathbf{u}|^2. \quad (3.9)$$

The maximal value of the ratio h_z/η_B is also given in table 1. It is less than or equal to 1.0

Ra	regime	Nu_{GL}	h^{BL}/H	Nu_{OB}^{DNS}	h/H	$\max(h_z/\eta_B)$	$N_r \times$	$N_\phi \times$	N_z
10^5	I_∞	4.7	57.6×10^{-3}	3.88 ± 0.01	14.1×10^{-3}	0.41	$32 \times$	$64 \times$	64
10^6	I_∞	7.6	19.9×10^{-3}	8.84 ± 0.02	12.3×10^{-3}	0.96	$32 \times$	$64 \times$	64
10^7	I_u	13.2	8.33×10^{-3}	17.62 ± 0.13	7.81×10^{-3}	1.04	$64 \times$	$128 \times$	128
10^8	I_u	25.6	3.00×10^{-3}	33.92 ± 0.61	2.60×10^{-3}	0.76	$192 \times$	$512 \times$	384
10^9	III_u	52.9	0.99×10^{-3}	65.38 ± 1.24	2.60×10^{-3}	1.60	$192 \times$	$512 \times$	384
10^9	III_u	52.9	0.99×10^{-3}	65.76 ± 0.74	1.30×10^{-3}	0.83	$384 \times$	$1024 \times$	768

TABLE 1. Rayleigh number Ra , the regime and Nusselt number Nu_{GL} according to the Grossmann–Lohse theory (Grossmann & Lohse 2000, 2001, 2002, see section 4.7 for details), the Nusselt number for the OB cases obtained in our simulations Nu_{OB}^{DNS} , the requested maximal cell size in the BLs h^{BL}/H , according to equation (3.7), and the actual one h/H , the maximal value of the ratio of the vertical mesh width to the Batchelor length $\max(h_z/\eta_B)$, and the number of nodes N_r , N_ϕ , N_z in the radial, azimuthal, and vertical direction, respectively.

for the whole computational domain and for all considered cases. These considerations show that our grid resolution has indeed been chosen properly.

4. Discussion of the flow under OB and NOB conditions

Rayleigh–Bénard convection is studied most often in low and moderate Prandtl number fluids, for example, air ($Pr = 0.7$) and water ($Pr = 4.38$). However, the flow in large Prandtl number fluids differs greatly from the flow at lower Prandtl numbers at the same Rayleigh number (see e.g. Wagner *et al.* 2012). This can be realised at first glance by looking at the instantaneous flow fields in figure 2.

We now discuss the results from a total of 17 simulations, that is, $Ra \in \{10^5, 10^6, 10^7, 10^8, 10^9\}$, each under OB conditions and the NOB condition $\Delta = 40$ K. For $Ra = 10^6$ we additionally performed NOB simulations for $\Delta \in \{10$ K, 20 K, 30 K, 50 K, 60 K, 70 K, 80 K $\}$. For all simulations we started temporal averaging when the flow had statistically converged. As the criterion for this, we waited for the radial and azimuthal averaged Nusselt number to be constant along the vertical coordinate after an appropriate averaging time. In general, this meant at least five thousand time units, but rather typically ten thousand time units before initiating and several thousand time units of actual statistical averaging. Thus, the statistical data for the higher Δ , i.e. 60 K–80 K, and higher Ra , i.e., 10^8 and 10^9 , were obtained within 1000 to 3000 time units, and for lower Δ and Ra , within more than 3000 and up to 10 000 time units.

4.1. Flow structures and plume dynamics

Following the classification by Krishnamurti & Howard (1981); Busse (1978); Getling (1998), and Manga & Weeraratne (1999), the flow behaviour in Rayleigh–Bénard convection can be distinguished into steady, unsteady, plume-dominated, transitional, and turbulent. Except for the fully turbulent case, our simulations covered all these flow regimes. The visualisation of the spatial structures can be used with relative ease as a method for distinguishing between the different states. Another criterion for categorising them is to use the probability density functions (PDFs), which will be discussed in section 4.4.

We present the instantaneous temperature fields for $Ra \in \{10^5, 10^6, 10^7, 10^8, 10^9\}$ in figure 2, and in addition, the time averaged temperature and velocity fields for the

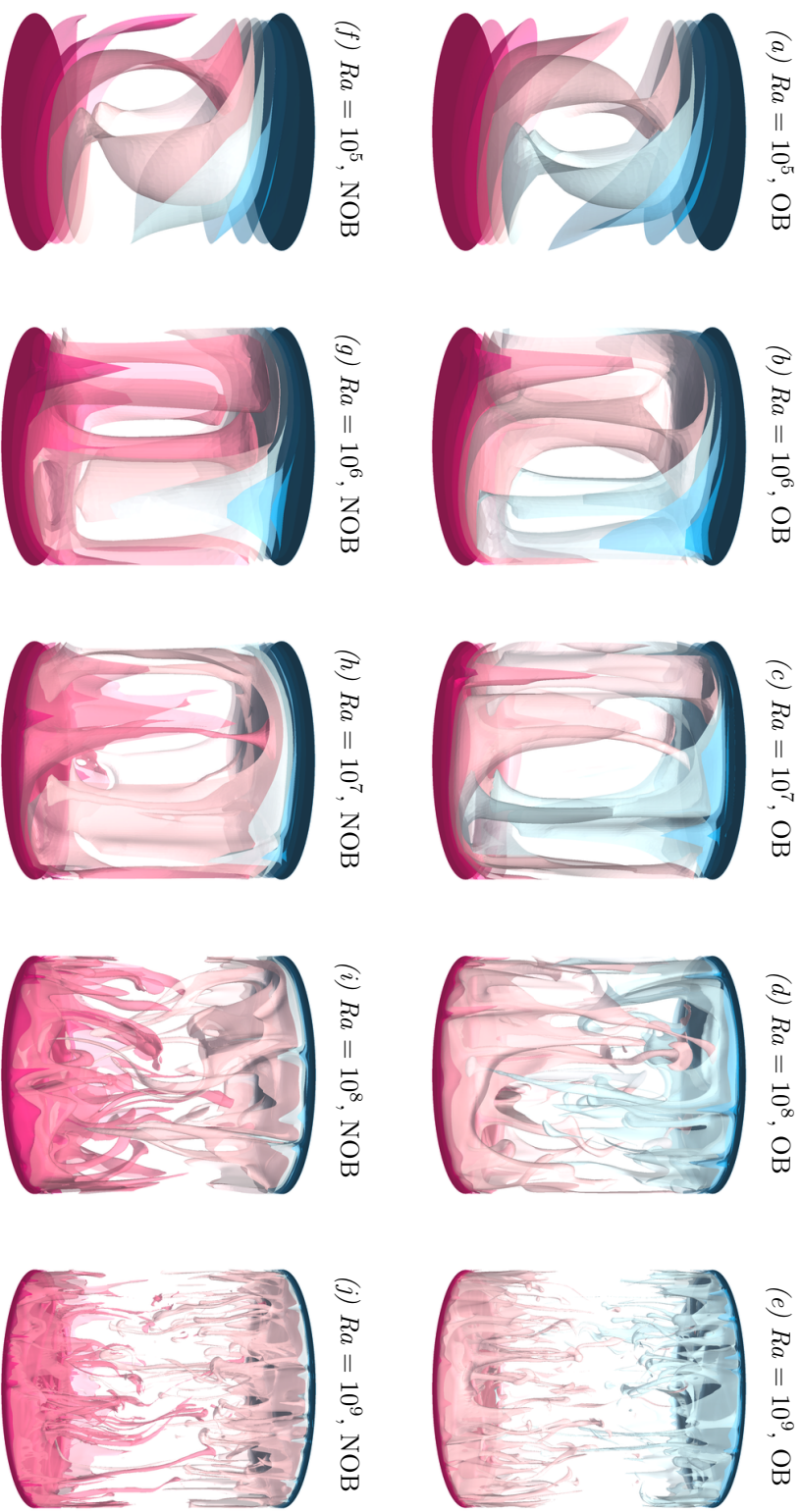


FIGURE 2. Instantaneous temperature isosurfaces under OB (figures (a)–(e)) and NOB ($\Delta = 40$ K, figures (f)–(j)) conditions for $Ra \in \{10^5, 10^6, 10^7, 10^8, 10^9\}$. Shown are ten isosurfaces, evenly spaced between the minimal and maximal values, i.e., pink indicates (dimensionless) temperatures above zero and blue temperatures below zero.

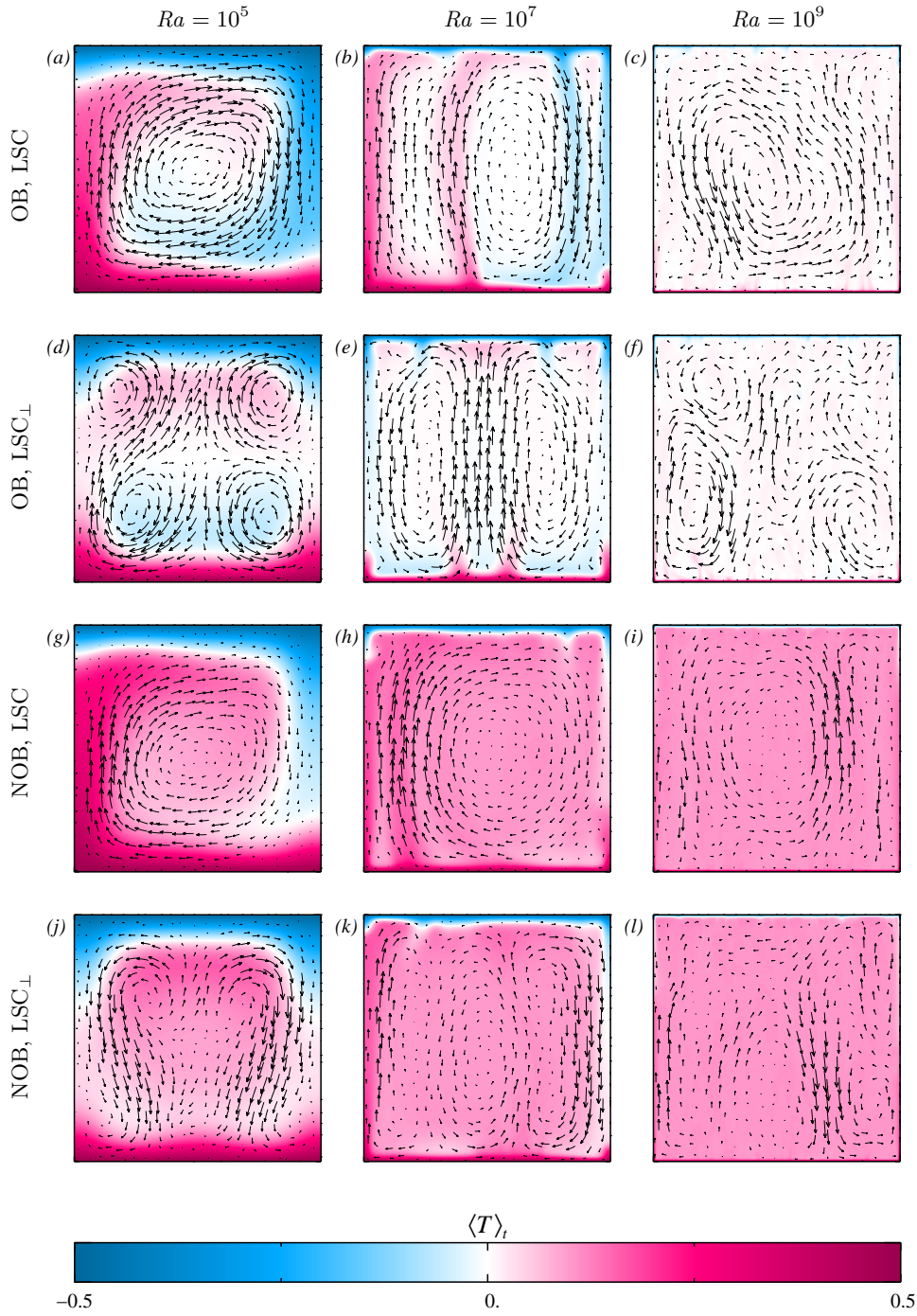


FIGURE 3. Time-averaged temperature fields with overplotted velocity field for $Ra = 10^5$ (first column), $Ra = 10^7$ (second column) and $Ra = 10^9$ (third column). The pictures are arranged in the following manner: the first and second row show the OB case, (a)–(c) is the plane where one convection roll or large scale circulation, respectively, is found (abbreviated by LSC), (d)–(f) the central vertical plane perpendicular to it (LSC_{\perp}); the third and the fourth row show the NOB case, again (g)–(i) is the plane of the LSC and (j)–(l) the plane LSC_{\perp} .

representative cases of $Ra = 10^5$, 10^7 , and 10^9 in figure 3 under both OB and NOB conditions with $\Delta = 40$ K.

For our lowest Rayleigh number, $Ra = 10^5$, and under OB conditions, we find a single convection roll. The time averaged 2D slices reveal a plane with one large roll and tiny counter-rotating secondary rolls at its edges. In the vertical plane perpendicular to it, four equally sized smaller convection rolls develop. The time averaged and the instantaneous flow fields are virtually the same. The temporal variation is only on a long time scale and we can speak of a three-dimensional flow with quasi-steady behaviour. A similar superposition of two roll patterns has been referred to as bimodal convection by Busse (1978), however, the sense of rotation of these patterns relative to each other is opposite to that reported by Busse (1979) for high Pr fluids. This disagreement might be an effect of the finite size of our cell. Under NOB conditions, the flow structures are similar, but the perfect top–bottom symmetry, typical for OB cases, is broken. We do not only obtain a clearly visible increase of the bulk temperature, but also a shifting of the large convection roll away from the centre. In the instantaneous flow field, we can also see that partially even the downwelling flow has a positive temperature, $T > 0$. Hence, the four rolls in the plane perpendicular to the large convection roll are arranged in a different manner. The upper two rolls are less extended in size and their centres are shifted closer to the cylinder axis, while the lower rolls are situated closer to the walls.

With increasing Rayleigh number, the flow becomes gradually unsteady and plumes start to rise from the boundary layers. Generally, they keep on being connected to their boundary layers where they are formed, until they reach the opposite cold or hot wall. However, the plumes become thinner with increasing Ra and thus also the number of emitted plumes increases. Their persistency is attributed to the domination of the diffusion of momentum over the diffusion of heat.

For $Ra = 10^6$ and 10^7 , single isolated plumes emerge. In the OB case, time averaging reveals three lengthy rolls extending in the vertical direction with very small rolls between them at the top and bottom. This three roll structure resembles the flow developing at higher aspect ratios and lower Prandtl numbers. An example for $Pr = 0.7$ and an aspect ratio of $\Gamma = 10$ was shown by Shishkina & Wagner (2006). A similar structure was also detected by Silano *et al.* (2010) for slightly different parameters, $Pr = 10^3$, $Ra = 10^8$ and $\Gamma = 0.5$. Under NOB conditions the flow is distorted similar to the case of $Ra = 10^5$: again the centre temperature is higher, we find warm down going plumes, and the large scale structures are arranged asymmetrically. In fact, one of the three rolls is much larger than the other two. Therefore, we can find a plane where it resembles a typical large scale circulation (LSC). However, in the plane perpendicular to it (LSC_{\perp}), the corresponding four-roll structure is missing. The 3D field confirms as well that the structure is more complex.

At $Ra = 10^8$ and $Ra = 10^9$, the highest Rayleigh numbers we could attain, we find a system where the velocity of the plumes and large-scale structures are comparable, leading to the impression that the flow is only governed by plumes, which cross the Rayleigh–Bénard cell almost unaffected. Thus, it seems reasonable to call this a plume-dominated regime. This was also described by Breuer *et al.* (2004) and Schmalzl *et al.* (2004). But even at $Ra = 10^9$, the majority of plumes are still connected to their thermal boundary layers: only a few detach from them. While the instantaneous fields have very distinct features, as pictured in figure 2 for $Ra = 10^8$ and 10^9 , the time averaged flow fields are very similar to the ones obtained for lower Pr at the same Ra . They unambiguously show an LSC. Again in the NOB case the overall flow pattern within the cylinder is more complex, but the general feature, i.e. the LSC is still present. Apparently, this behaviour has not been found in the 2D simulations by Sugiyama *et al.* (2007), neither in the OB

nor in the NOB case. Hence, 3D simulations are necessary to capture all the relevant flow structures, especially for NOB effects. Our findings are also more consistent with the results of the experiments for $Ra = 2.3 \times 10^8$ by Zhang *et al.* (1997), although all plumes stayed connected with their boundary layer and the LSC was easier to recognise in the experiments. The reason for this disagreement is probably the about half as large Pr in their case.

We would also like to emphasize that during averaging, we could neither find any reversals of the LSC nor any noticeable shifting of the azimuthal angle of the large scale structures. While all the presented flow fields display a clearly chaotic behaviour, the transition range to a fully developed turbulent flow extends up to $Ra \approx 10^{12}$ when using the criterion based on the average Kolmogorov length as a typical length scale for the coherent structures.

Many of the asymmetries obtained in the NOB cases can be ascribed to the different viscosities in the cold top and hot bottom layers. That is, the lower viscosity at the warm bottom makes the plumes more prone to leave the bottom layer and they are also more mobile, i.e., faster. The cold plumes from the top have the exact opposite behaviour: they are very viscous and thus rather remain within the cold top boundary layer. Or alternatively, one could say that the plumes emanating from the cold top layer move more slowly and hence, they remain much longer in contact with the ambient medium in the bulk and heat up on their way down. These asymmetric plume dynamics have a significant influence on the entire flow behaviour and, in particular, on the boundary layers and the temperature profiles. This will be explained in more detail in the following sections.

4.2. Mean temperature profiles and thermal boundary layers

Figure 4 presents the time and r - ϕ plane averaged mean temperature profiles under OB and NOB conditions. Figure 4(a) shows the profiles for different Ra under OB and under NOB conditions, each time for $\Delta = 40$ K. In figure 4(b) the Rayleigh number is kept constant at $Ra = 10^6$ and various NOB conditions, i.e., Δ , are shown.

At the beginning of our simulations, all profiles exhibited an overshoot adjacent to the BLs. Schmalzl *et al.* (2004), amongst others, observed this feature already at $Pr = 100$ for $Ra = 10^6$, and suggested that this is a feature of the high Prandtl number. In our case, however, both under OB and NOB conditions, those overshoots disappeared in the course of our simulations. Thus, we think that this intermediate phenomenon is rather an indicator that the statistical equilibrium state has not been reached yet. Nonetheless, in the profiles for $Ra = 10^5$ and $Ra = 10^6$, seen in figure 4 (a)–(b), some non-monotonicity persists due to the occurring structures (cf. figure 10) in this still quasi-steady regime and is not expected to disappear after even longer averaging times. We will follow up on this in section 4.5.

The most prominent feature that distinguishes the NOB profiles from the OB ones is the higher temperature in the bulk. The deviation of the centre temperature T_c from the arithmetic mean temperature will be treated in detail in section 4.3. Furthermore, the NOB profiles always lie above the corresponding OB profiles, i.e., they bend more towards the plate temperature close to the top and further away from the plate temperature close to the bottom, in comparison to the OB profiles. It is more easily visible when looking at the second derivative where the profiles are normalised by the maximum absolute value of the second derivative of the corresponding OB profile,

$$\varkappa = \frac{1}{\max |\varkappa_{OB}|} \left\langle \frac{\partial^2 T}{\partial z^2} \right\rangle_{r,\phi,t}, \quad (4.1)$$

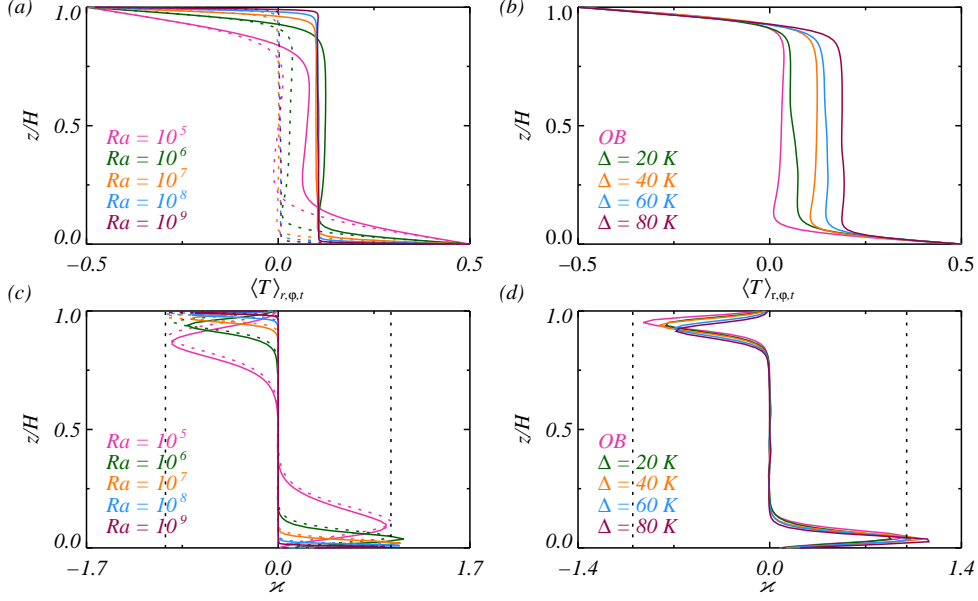


FIGURE 4. (a)–(b) Mean temperature profiles, i.e., the temperature averaged in time t and in every r – ϕ plane. (c)–(d) Curvature of the temperature profiles normalised to the OB value, as defined by equation (4.1). The black dashed vertical lines mark the points where $|z| = 1$. The left panels (a) and (c) correspond to varying Ra and the dashed lines indicate the OB case and the solid lines the NOB cases for $\Delta = 40$ K. The right panels (b) and (d) correspond to a constant $Ra = 10^6$ and each time the OB case and various NOB conditions, i.e., $\Delta \in \{20 \text{ K}, 40 \text{ K}, 60 \text{ K}, 80 \text{ K}\}$.

seen in figures 4(c) and (d). Close to the top plate we have $|z| < 1$ and close to the bottom one we have $|z| > 1$. This behaviour is enhanced with increasing Δ as well as with increasing Ra . A similar result was obtained for water by Ahlers *et al.* (2006). The reason lies in the larger heat conductivity Λ at the bottom and the smaller Λ at the top. Since the heat flux has to be same at both boundaries, the temperature profiles have to compensate for this.

Associated with the profiles are the different thicknesses of the boundary layer. The thermal boundary layer thicknesses λ_t^θ and λ_b^θ are defined by means of the profile's slope at the top ($z = H$) and bottom plate ($z = 0$), and are thus called the slope thicknesses. That is, the distance from where the tangent to the mean temperature profile at the top or bottom, respectively, intersects with the isoline of the centre temperature T_c ,

$$\lambda_t^\theta = \left(\frac{\partial \langle T \rangle_{r,\phi,t}}{\partial z} \Big|_t \right)^{-1} (T_t - T_c), \quad (4.2)$$

$$\lambda_b^\theta = \left(\frac{\partial \langle T \rangle_{r,\phi,t}}{\partial z} \Big|_b \right)^{-1} (T_c - T_b). \quad (4.3)$$

The ratio of the top to bottom BL thickness, $\chi_\lambda^\theta = \lambda_t^\theta / \lambda_b^\theta$, is given in figure 5. It is practically independent of Ra , but increases with increasing Δ , i.e., the top thermal boundary layer is always thicker than the bottom one, $\lambda_t^\theta > \lambda_b^\theta$. For the highest considered temperature difference, $\Delta = 80$ K, the top BL is about 2.5 times thicker.

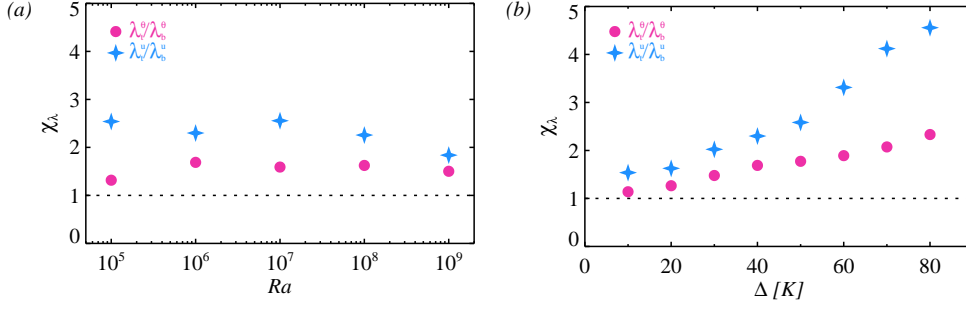


FIGURE 5. (a) Ratio of the top to bottom thermal (χ_λ^θ) and viscous (χ_λ^u) BL thicknesses, for constant $\Delta = 40$ K, as functions of Ra . The dashed line indicates the point where the top and bottom BL have the same thickness, i.e. $\chi_\lambda = 1$. (b) Similar to figure (a) but for constant $Ra = 10^6$, as functions of Δ .

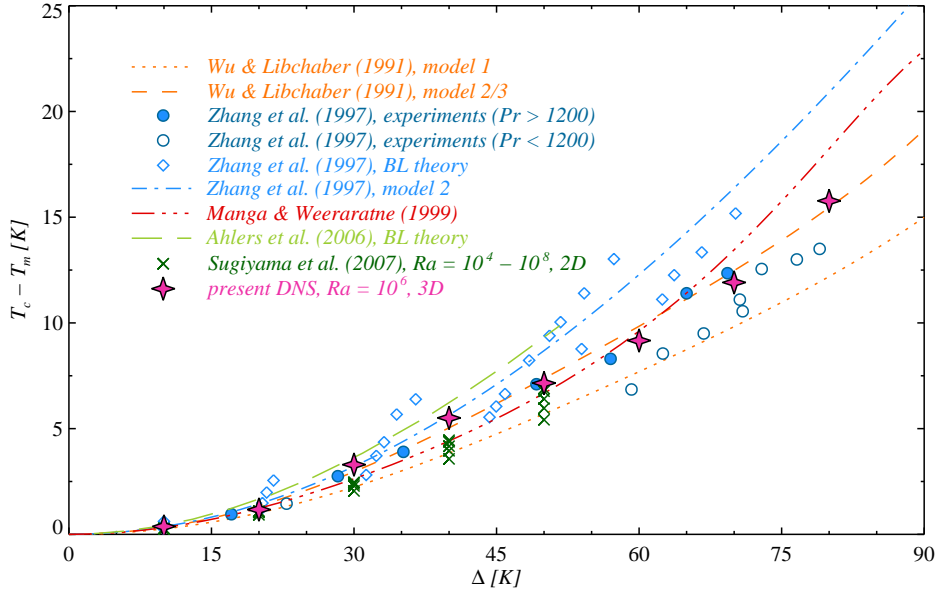


FIGURE 6. The centre temperature T_c vs. Δ for a fixed $Ra = 10^6$, the predictions from the models of Wu & Libchaber (1991), Zhang *et al.* (1997), Manga & Weeraratne (1999), and Ahlers *et al.* (2006), and the results from 2D simulations by Sugiyama *et al.* (2007) are plotted as well.

4.3. Centre temperature T_c

One of the best known, and also best analysed, NOB phenomena is the deviation of the temperature in the centre T_c from the arithmetic mean temperature T_m . Our three-dimensional DNS showed that for a temperature difference of $\Delta = 80$ K, the centre temperature can be up to 15 K higher than under OB conditions.

There exist several models to predict the change of T_c , amongst others there are the ones by Wu & Libchaber (1991), Manga & Weeraratne (1999), and Ahlers *et al.* (2006). The comparison of the model predictions to our DNS data is shown in figure 6. Most of the models considered here are essentially based on the following ideas. In the centre of the cell, the heat is almost solely transported by convection, but in the boundary layers by conduction, since there the velocity approaches zero. Because the total dimensionless heat flux, i.e., the Nusselt number Nu , is the sum of the convective and conductive heat

fluxes, q_{conv} and q_{cond} ,

$$Nu = q_{conv} + q_{cond} = (RaPr\gamma)^{1/2} \langle u_z T \rangle - \gamma^{-1} \left\langle \Lambda \frac{\partial T}{\partial z} \right\rangle, \quad (4.4)$$

it needs to be constant due to energy conservation. The temperature gradient is zero in the bulk, hence the mean temperature $\langle T \rangle_{r,\phi,t}$ only changes within the boundary layers, and thus the total temperature drop Δ is the sum of the temperature drops within the top and the bottom boundary layers:

$$\Delta = \Delta_t + \Delta_b. \quad (4.5)$$

Obviously, the ratio

$$\chi_\Delta = \frac{\Delta_t}{\Delta_b} \quad (4.6)$$

equals one under OB conditions, but in the NOB case this is no longer true. It will prove to be convenient to combine these two equations and express the two temperature drops as follows:

$$\Delta_t = \frac{\chi_\Delta}{1 + \chi_\Delta} \Delta, \quad (4.7)$$

$$\Delta_b = \frac{1}{1 + \chi_\Delta} \Delta. \quad (4.8)$$

In the thermal boundary layers the heatflux is given by conduction, hence

$$q_{cond} = \Lambda_{\bar{t}} \frac{\Delta_t}{\lambda_t^\theta} = \Lambda_{\bar{b}} \frac{\Delta_b}{\lambda_b^\theta} \quad \Rightarrow \quad \kappa_{\bar{t}} \frac{\Delta_t}{\lambda_t^\theta} = \kappa_{\bar{b}} \frac{\Delta_b}{\lambda_b^\theta}. \quad (4.9)$$

The indices \bar{t} and \bar{b} here and in the following denote that the quantity is taken at the interpolated temperatures $(T_t + T_c)/2$ and $(T_b + T_c)/2$. The latter equality in (4.9) results from the fact that ρ and c_p are assumed to be constant over the cell. In our opinion, a better prerequisite is the exact relation at the plates, i.e.,

$$q_{cond} = \Lambda_t \frac{\Delta_t}{\lambda_t^\theta} = \Lambda_b \frac{\Delta_b}{\lambda_b^\theta} \quad \Rightarrow \quad \kappa_t \frac{\Delta_t}{\lambda_t^\theta} = \kappa_b \frac{\Delta_b}{\lambda_b^\theta}. \quad (4.10)$$

Nonetheless, Wu & Libchaber (1991) used (4.9), since the latter equation (4.10) results in a greater deviation from their experimental data for all their T_c models. We came to the same conclusion with our numerical data.

In the first model, they assume that the boundary layer Rayleigh number is the same at the top and bottom,

$$Ra_{\bar{t}} = Ra_{\bar{b}} \quad \Leftrightarrow \quad \frac{\alpha_{\bar{t}} g \Delta_t \lambda_t^3}{\kappa_{\bar{t}} \nu_{\bar{t}}} = \frac{\alpha_{\bar{b}} g \Delta_b \lambda_b^3}{\kappa_{\bar{b}} \nu_{\bar{b}}}. \quad (4.11)$$

Their second proposed model follows the scaling model of Castaing *et al.* (1989) and assumes that the velocity scales w of the plumes are equal,

$$w_{\bar{t}} = w_{\bar{b}} \quad \Leftrightarrow \quad \frac{g \alpha_{\bar{t}} \Delta_t \lambda_t^2}{\nu_{\bar{t}}} = \frac{g \alpha_{\bar{b}} \Delta_b \lambda_b^2}{\nu_{\bar{b}}}. \quad (4.12)$$

These scales are based on the balance between the buoyancy force $g\alpha\Delta$ and the viscous force $\nu w/\lambda^2$. The third model will yield the same result, and is again based on the aforementioned scaling model, but this time assuming the same temperature scales Θ

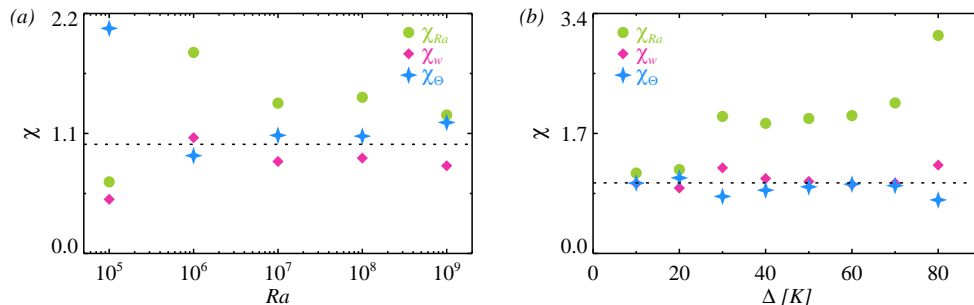


FIGURE 7. (a) The left panel shows different ratios of top to bottom quantities, the BL Rayleigh numbers χ_{Ra} , the plume velocity scales χ_w , and the temperature scales χ_Θ as functions of Ra for the NOB simulations with $\Delta = 40$ K. (b) The right panel shows the same quantities but as functions of Δ for fixed $Ra = 10^6$. The dashed line corresponds to $\chi = 1$ in each case.

within the boundary layers,

$$\Theta_{\bar{t}} = \Theta_{\bar{b}} \quad \Leftrightarrow \quad \frac{\kappa_{\bar{t}} \nu_{\bar{t}}}{g \alpha_{\bar{t}} \lambda_{\bar{t}}^3} = \frac{\kappa_{\bar{b}} \nu_{\bar{b}}}{g \alpha_{\bar{b}} \lambda_{\bar{b}}^3}. \quad (4.13)$$

All these assumptions can be checked against our DNS data. Figure 7 presents the ratios

$$\chi_{Ra} = \frac{Ra_{\bar{t}}}{Ra_{\bar{b}}}, \quad \chi_w = \frac{w_{\bar{t}}}{w_{\bar{b}}} \quad \text{and} \quad \chi_\Theta = \frac{\Theta_{\bar{t}}}{\Theta_{\bar{b}}}. \quad (4.14)$$

We find that in the case of glycerol and the ranges of Ra and Δ considered here, none of the assumptions is perfectly fulfilled. Wu & Libchaber (1991), however, found that at least the ratio χ_Θ of the third model was constant in their experiments conducted for low-temperature helium gas, while the assumptions for the first and second model did not hold.

Even though none of the required conditions are perfectly met, the models give a good prediction of the actual T_c for glycerol. We can complete equations (4.5) and (4.9) now with either equation (4.11), (4.12), or (4.13), and uniquely calculate the ratio χ_Δ ,

$$\chi_{\Delta,1} = \left(\frac{\alpha_{\bar{b}} \nu_{\bar{t}}}{\alpha_{\bar{t}} \nu_{\bar{b}}} \right)^{1/4} \left(\frac{\kappa_{\bar{b}}}{\kappa_{\bar{t}}} \right)^{1/2}, \quad (4.15)$$

$$\chi_{\Delta,2/3} = \left(\frac{\alpha_{\bar{b}} \nu_{\bar{t}}}{\alpha_{\bar{t}} \nu_{\bar{b}}} \right)^{1/3} \left(\frac{\kappa_{\bar{b}}}{\kappa_{\bar{t}}} \right)^{2/3}. \quad (4.16)$$

All of the material properties still depend on χ_Δ , but with the help of the polynomial functions of the material properties these equations can be easily solved numerically. Herewith, and using equations (4.7) and (4.8), the centre temperature T_c can be calculated:

$$T_c = T_t + \Delta_t = T_b - \Delta_b. \quad (4.17)$$

The difference $T_c - T_m$ for the three models is shown for different Δ in figure 6.

Zhang *et al.* (1997) used a two-dimensional steady-state boundary layer model with three main assumptions. First, the plumes transport not between the thermal top and bottom layer but only from the walls to the mixing region between the layers. Second, T_c is adjusted, so that the fluxes at the top and bottom are equal, and third, the viscous stress is constant within the thermal sublayer. Then the laminar two-dimensional thermal boundary layer equation is solved numerically. The result yields T_c as a function of both T_t and T_b . However, they only took into account the temperature dependency of the viscosity and not the thermal diffusivity. Zhang *et al.* (1997) also gave another approximation for

the third model of Wu & Libchaber (1991) consistent with their BL theory. Using an exponential dependency of the viscosity, i.e., $\nu(T) \propto \exp(-cT)$, $c = 0.087$, and again leaving all the other material properties constant, they found the fit

$$T_c = \frac{\Delta}{2} \tanh(c\Delta/12). \quad (4.18)$$

They also conducted experiments and measured the centre temperature. Certain points for their BL model, the tanh fit (4.18) and the experimental data are shown in figure 6 as well. In their experiments the mean temperature T_m varied strongly, between 24.55°C and 64.75°C , and hence, so did the Prandtl number, between approximately 600 and 8000. As consequence, the scatter of T_c is large. Thus, we distinguished between $Pr > 1200$ and $Pr < 1200$. The data points for higher Pr show a very good agreement with our three-dimensional DNS data. On the contrary, the lower Pr data yield a lower T_c .

Manga & Weeraratne (1999) investigated Rayleigh–Bénard convection in corn syrup which has a comparable high Prandtl number between $10^3 < Pr < 10^6$ and a similar temperature-dependent viscosity. By also considering an exponential dependency of the viscosity, assuming that Nu scales with the Péclet number $Pe = PrRe$ with $Nu \propto Pe^{-1/3}$ and that the temperature drop within the convecting region is $\Delta/2$ (which is equivalent to using $T_{\bar{t}}$ and $T_{\bar{b}}$), they found the following relation for the centre temperature,

$$T_c = \frac{\Delta}{1 + \left(\frac{\nu_t}{\nu_b}\right)^{-1/6}} + T_t, \quad (4.19)$$

also presented in figure 6.

Ahlers *et al.* (2006) used a similar approach to Zhang *et al.* (1997), but extended the Prandtl–Blasius BL theory also for a temperature-dependent diffusivity κ . In figure 6 we extended it for Δ up to 80 K to get a better impression of the actual validity of this approach for higher temperature differences, for which also most of the measurements of Zhang *et al.* (1997) had been performed. The comparison with the experimental and our DNS data revealed that the 2D boundary layer models overestimate the actual T_c . The rather poor agreement—at least in comparison to its very successful application in the case of water—can be explained easily. As already pointed out by Sugiyama *et al.* (2009) the main deviation is caused by plume emission. However, in the case of glycerol, this happens not only close to the walls, but indeed everywhere on the plates, making the Prandtl–Blasius BL theory less applicable. The discrepancy gets worse due to the fact that the plumes stay connected to their BLs.

Finally, we also show in figure 6 the data from the two-dimensional simulations by Sugiyama *et al.* (2007). Their data are lower than ours, even though we have chosen the same Pr . Assuming that the scatter in the experimental data is indeed caused by different Pr , it seems to us that two-dimensional simulations are insufficient for obtaining an accurate value of T_c .

In conclusion, the model of Wu & Libchaber (1991) based on the same velocity or temperature scale in the top and bottom boundary layer (equations (4.12)–(4.13)) predicts T_c the best out of all the considered models, with a standard deviation of 0.4 K.

4.4. Probability density functions of the temperature

Figure 8(a) presents the volume-weighted probability density functions (PDFs) of the time averaged temperature for the whole cell. In the OB cases, the most likely temperature is the arithmetic mean temperature T_m , while in the NOB cases the most likely temperature is close to T_c . The change of the PDFs, i.e., the shift to the right, is also associated with the presence of thermal BLs with different thicknesses. Figure 8(b) shows

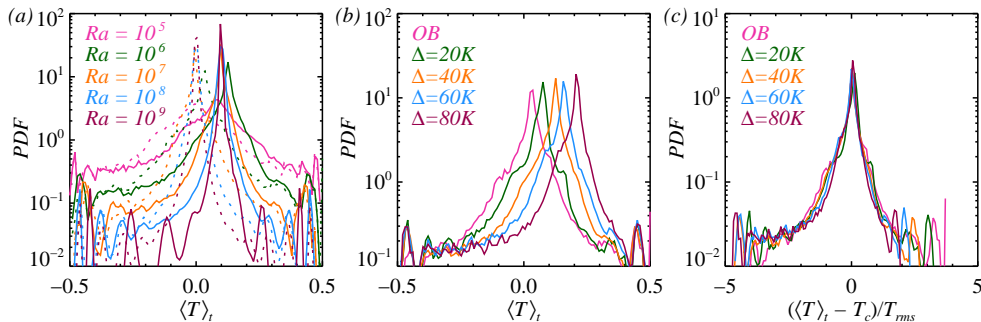


FIGURE 8. Probability density functions (PDFs) of the time averaged temperature for the whole volume. (a) Different Ra , the dashed line indicates the OB case, the solid line the NOB case with $\Delta = 40$ K. (b) Constant $Ra = 10^6$, shown are the OB case and four different NOB cases.

the PDFs for a constant Ra but varying Δ ; the PDFs become more asymmetric and the maximum peak is shifted to higher temperatures.

Following the classification of Manga & Weeraratne (1999), we can herewith also distinguish between the different styles of convection. If the distribution is Gaussian, then we expect the flow to be quasi-steady. If the distribution is exponential, then we are in the turbulent regime. However, for high Prandtl number fluids, these curves have superimposed on them a persisting peak caused by the plumes (cf. e.g. Manga & Weeraratne 1999). Thus, for $Ra = 10^5$ the PDF is Gaussian, while with increasing Ra the plumes become more predominant, resulting in a more and more prominent peak. When Ra is increased further ($Ra \gtrsim 10^9$), the background starts to resemble an exponential distribution and the plume-induced peak starts to gradually vanish. For the fully developed turbulent regime, we expect the shape of the PDFs to become completely exponential.

4.5. Wind profiles and viscous boundary layers

The very distinct large scale structures occurring in glycerol can also be detected by looking at the profiles of the radial and vertical velocity components and the rms velocity fluctuations. The rms velocity fluctuations, or turbulence intensities, are defined by

$$u_{rms} = (\langle u^2 \rangle_t - \langle u \rangle_t^2)^{1/2}, \quad (4.20)$$

where u denotes one of the three velocity components, u_r , u_ϕ or u_z .

We show the radial and vertical velocity profiles for $10^5 \leq Ra \leq 10^9$ under OB and the NOB condition $\Delta = 40$ K in figure 9(a), and likewise for $Ra = 10^6$ and various NOB conditions $\Delta = 20$ K, 40 K, 60 K and 80 K in figure 9(b). The radial profiles are obtained by averaging $u_z(r, \phi, z)$ in time and along ϕ and z and are thus functions of the radial position, i.e., $\langle u_z \rangle_{\phi, z, t}(r)$. Similarly, the vertical profiles are obtained by averaging $u_r(r, \phi, z)$ in time and along r and ϕ and are thus functions of the vertical position, i.e., $\langle u_r \rangle_{r, \phi, t}(z)$. The radial profiles can generally be considered to be relevant for the wind along the plates, whereas the vertical profiles are relevant for the wind being parallel to the bottom and top plate.

However, the flow patterns for glycerol are more complex than just a single LSC with cornerflows, thus the profiles' appearance does not resemble the one detected at lower Pr . That means we cannot find small negative or positive values in the vicinity of the walls caused by cornerflows, but instead we find several maxima in the vertical profiles, and not all the radial profiles are zero at the centre line of the cylinder. Furthermore, as can be seen in figure 2 and 3, there is an upwelling structure approximately in the centre

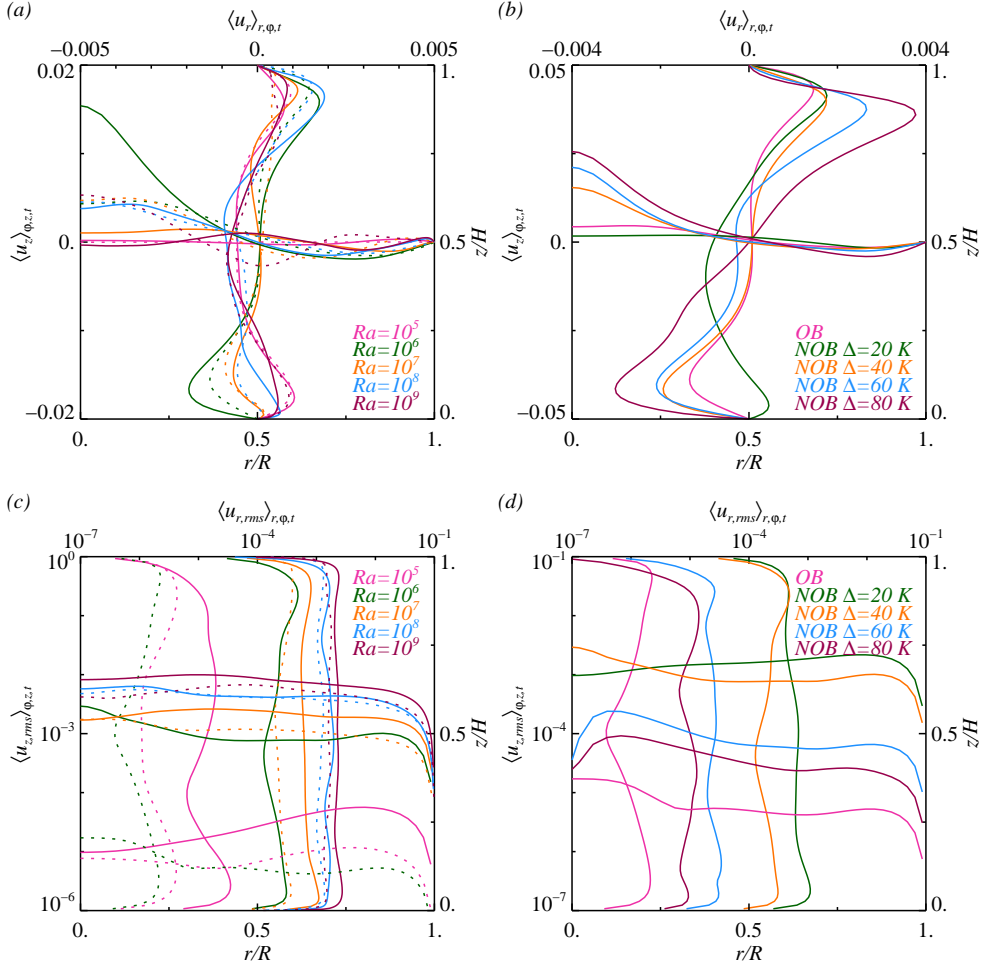


FIGURE 9. (a) Mean profiles of the radial velocity $u_r(z)$ and the vertical velocity $u_z(r)$ for different Ra . The dashed lines indicate the OB, the solid lines the NOB cases with $\Delta = 40\text{ K}$. (b) Similar to (a), but for constant $Ra = 10^6$ and different NOB cases, i.e., Δ , as well as under OB conditions. (c) Mean profiles of the radial rms velocity $u_{r,rms}(z)$ and the vertical rms velocity $u_{z,rms}(r)$ for different Ra . The dashed lines indicate the OB, the solid lines the NOB cases with $\Delta = 40\text{ K}$. (d) Similar to (c) but for $Ra = 10^6$ and different NOB cases, i.e., Δ , as well as under OB conditions.

of the cylinder for $10^6 \leq Ra \leq 10^8$, under both OB and NOB conditions. Thus, close to the bottom plate, the radial flow is direct inwards, i.e. $\langle u_r \rangle_{r,\phi,t} < 0$, feeding the central structures, and then when reaching the top, the flow is consequently, directed outwards, i.e., $\langle u_r \rangle_{r,\phi,t} > 0$.

The major difference in the NOB case is, that the vertical profiles are bent further away from the plate near the top, and closer towards it near the bottom compared to the OB profiles, i.e., exactly the opposite from the case for the temperature profiles. The reason is the different boundary layers, where also the largest variations of the material properties occur. But generally, we cannot find a clear trend in which way the profiles are modified under NOB conditions. This is especially evident in the case of $Ra = 10^6$. For $\Delta = 20\text{ K}$ the velocity $\langle u_z \rangle_{\phi,z,t}(r = 0)$ is close to zero and lower than in the OB case,

while for higher temperature differences Δ the velocity at the centre line is higher than in the OB case. The vertical profiles show a similar peculiar behaviour.

To understand this, we can look at the instantaneous temperature fields for OB conditions and various NOB conditions, figure 2(b), (g) and 10. Depending on the imposed Δ , a different number of cells develop, whose shapes are also clearly influenced by the cylinder wall. While for $\Delta = 20$ K only two cells are present, a large one filling almost the whole cylinder and a very small one adjacent to it, the number of cells increases with Δ . Thus, there are three cells for $\Delta = 40$ K, four for $\Delta = 60$ K, and five for $\Delta = 80$ K. Remarkably, also under OB conditions, three cells develop, the same as for $\Delta = 40$ K. Except for $\Delta = 20$ K, we always find a coherent structure in the middle of the cell with a strong velocity component u_z directed upwards, explaining the different behaviours.

To further analyse why a different number of cells develops we need to examine the viscous boundary layers. However, the slope criterion (e.g. Wagner *et al.* 2012) turned out to be inapplicable in the case of glycerol. Especially for higher Δ , the velocity profiles bend so much away from the top plate, as depicted in figure 9(b), that the top BL thickness would be much thicker than $H/2$, which is not realistic. Thus, we decided to define the thickness of the viscous boundary layer as the vertical distance from the top and bottom plate, respectively, where the temporally averaged radial rms velocity profile $\langle u_{r,rms} \rangle_{r,\phi,t}$ reaches the first maximum,

$$\lambda_t^u = \max \left(z \mid \frac{\partial \langle u_{r,rms} \rangle}{\partial z} = 0 \right), \quad (4.21)$$

$$\lambda_b^u = \min \left(z \mid \frac{\partial \langle u_{r,rms} \rangle}{\partial z} = 0 \right). \quad (4.22)$$

The viscous boundary layers are thicker than the thermal ones, but show a similar asymmetry when NOB effects come into play. The reason for the asymmetry is that $\partial\nu/\partial T < 0$, and thus we have a thinner viscous boundary layer at the bottom and a thicker one at the top, which also induces correspondingly different thermal BLs. The ratios of top to bottom boundary layers, $\chi_\lambda^u = \lambda_t^u/\lambda_b^u$, as function of Ra and Δ are displayed in figure 5. χ_λ^u virtually does not depend on Ra , but increases with Δ , and reaches a maximum value of about 4.5 for $\Delta = 80$ K. The dependence of the ratio on Δ shows certain discontinuities, which agree with the points where one more cell appears, and thus implies a close connection. The increase of χ_λ means that the top boundary layer becomes thicker while the bottom one does not decrease in the same measure. We hypothesize, that this is the source of the different flow phenomenology, i.e., the different number of cells, occurring for different Δ : the effective volume where convection takes place and hence the effective aspect ratio is modified, and consequently the flow phenomenology.

Figure 9(c) and (d) show the rms profiles for the velocity components normal to the walls and parallel to it, $\langle u_{r,rms} \rangle_{r,\phi,t}(z)$ and $\langle u_{z,rms} \rangle_{r,\phi,t}(r)$, again for various Ra and under OB and NOB conditions and for $Ra = 10^6$ and various Δ , respectively. In the OB case there is a jump of two orders of magnitude between 10^6 and 10^7 in both rms values, consistent with our qualitative observation that starting from $Ra = 10^7$ plumes are emitted in a more random manner. Furthermore, the fluctuations in the velocity are higher in all NOB cases.

Alternatively, we also introduce wind profiles based on the specific kinetic energy similar to Sugiyama *et al.* (2009),

$$U^E = \sqrt{\frac{1}{2} \left(u_r^2 + u_\phi^2 + u_z^2 \right)}. \quad (4.23)$$

They are presented in figure 11. Since they combine all velocity components, these profiles

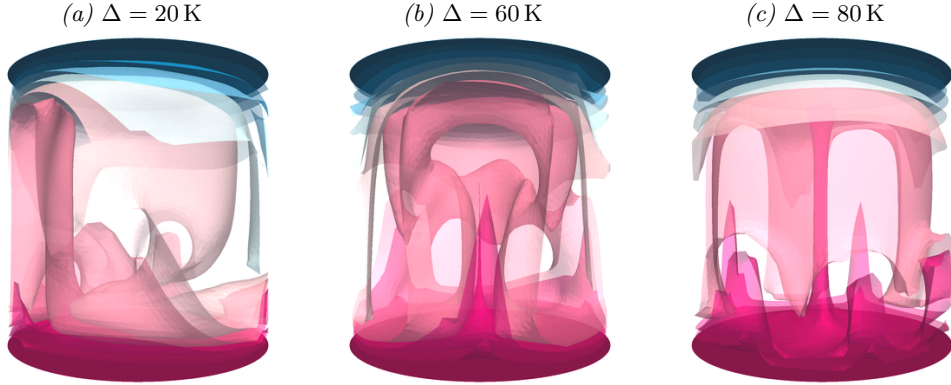


FIGURE 10. Instantaneous temperature isosurfaces for $Ra = 10^6$ under various NOB conditions, (a) $\Delta = 20$ K, (b) $\Delta = 60$ K, (c) $\Delta = 80$ K. Shown are ten isosurfaces, evenly spaced between the minimal and maximal value, i.e. pink indicates (dimensionless) temperatures above zero and blue temperatures below zero. The corresponding temperature fields for OB conditions and $\Delta = 40$ K can be seen in figure 2(b) and (g).

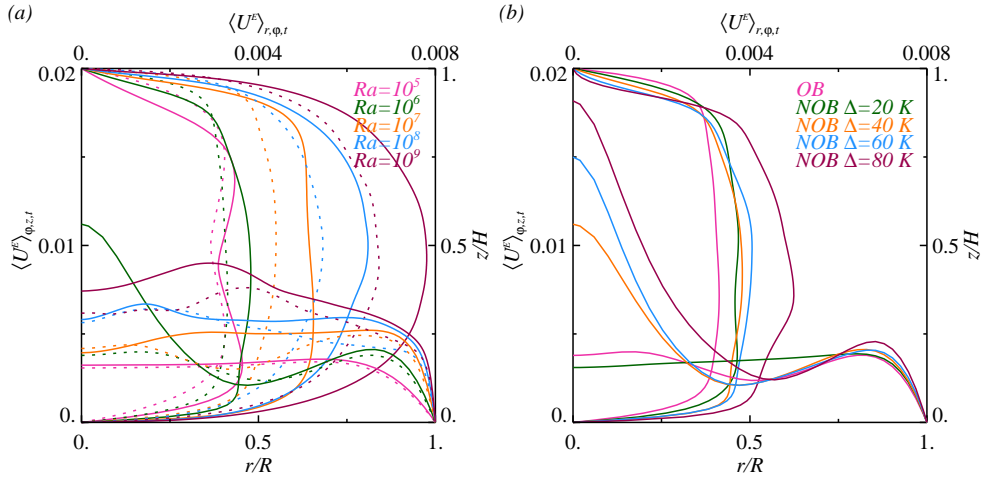


FIGURE 11. Energy based wind profiles as function of r and z . (a) For different Ra . The dashed lines indicate the OB, the solid lines the NOB cases with $\Delta = 40$ K. (b) Similar to (a), but for constant $Ra = 10^6$ and different NOB cases, i.e., Δ , as well as under OB conditions.

are rather global and give a good overall impression. Hence they should be less sensitive to the actual developing flow modes, but still be sensitive to NOB effects. Indeed, the profiles have similar asymmetries to the ones presented in figure 9, but in figure 11(b) some of the peculiarities of the NOB case $Ra = 10^6$ and $\Delta = 20$ K disappear, i.e., the profiles at the top $z/H = 1$ are arranged in sequence with Δ away from the upper plate and the profiles at the bottom $z/H = 0$ are arranged in sequence closer to the lower plate.

4.6. Reynolds number

With our knowledge about the wind profiles, we can now analyse one important outcome parameter of Rayleigh–Bénard simulations, the Reynolds number Re . Its definition includes a characteristic velocity, length and viscosity scale. A reasonable choice for the

characteristic length scale is the cylinder’s height H , while the characteristic viscosity and the characteristic velocity are less evident and are to be determined. They can be chosen differently and thereby crucially influence the value of Re . The Reynolds number expressed within our chosen reference dimensions is

$$Re = \frac{URa^{1/2}\gamma^{1/2}}{\nu Pr^{1/2}}. \quad (4.24)$$

We have analysed the Reynolds number Re^{pl} , based on the absolute peak value of the time averaged vertical velocity,

$$U = U^{pl} = \max |\langle u_z \rangle_t|, \quad (4.25)$$

representing a maximal plume speed, as suggested by Silano *et al.* (2010), and the Reynolds number Re^E , based on the volume averaged specific kinetic energy,

$$U = U_{\text{it}}^E = \sqrt{\left\langle \frac{1}{2} (u_r^2 + u_\phi^2 + u_z^2) \right\rangle_{V,t}}, \quad (4.26)$$

as was done by Sugiyama *et al.* (2009). Since the increased centre temperature leads to a smaller viscosity in the bulk, we also distinguish between Re_c defined with the viscosity ν_c and Re_m defined with the viscosity ν_m .

As shown in figure 12 (b), the absolute value of Re^{pl} is always greater than Re^E . But there is only a minor influence of the different reference viscosities ν_m and ν_c for $\Delta = 40$ K and the phenomenological behaviour is almost unaffected by it. However, Re^{pl} and Re^E differ not only in magnitude, but also in their scaling behaviour. We have performed power-law fits, $Re = cRe^\gamma$, in the range of $10^5 \leq Ra \leq 10^9$ for all defined Reynolds numbers and the results are shown in the legend of figure 12(a). We have also calculated the effective scaling in this range according to the Grossmann–Lohse theory (see esp. Grossmann & Lohse 2002; Ahlers *et al.* 2009), i.e., we have solved

$$(Nu - 1) Ra Pr^{-2} = c_1 \frac{Re^2}{g\left(\sqrt{\frac{Re_c}{Re}}\right)} + c_2 Re^3, \quad (4.27)$$

$$Nu - 1 = c_3 Re^{1/2} Pr^{1/2} \left[f\left(\frac{2aNu}{\sqrt{Re_c}} g\left(\sqrt{\frac{Re_c}{Re}}\right)\right) \right]^{1/2} + c_4 Pr Re f\left(\frac{2aNu}{\sqrt{Re_c}} g\left(\sqrt{\frac{Re_c}{Re}}\right)\right) \quad (4.28)$$

with the coefficients $a = 0.482$, $Re_c = 1.041$, $c_1 = 8.685$, $c_2 = 1.441$, $c_3 = 0.462$, $c_4 = 0.013$, and the crossover functions

$$f(x) = (1 + x^n)^{-1/n} \quad \text{and} \quad g(x) = x(1 + x^n)^{-1/n} \quad (n = 4). \quad (4.29)$$

The resulting curve under OB conditions is shown as well.

For Re^E , simple power laws are appropriate to capture the scaling of Re within the range of Ra considered. The $1-\sigma$ uncertainty estimates of the fit are at most 2% and there is no significant difference in the scaling exponents of Re_{OB}^E , Re_m^E , and Re_c^E . On the other hand, Re^{pl} does not obey a power law. We clearly see that a linear fit on a double-logarithmic scale does not reflect the behaviour of Re^{pl} with Ra . Indeed, this is also obtained within the framework of the Grossmann–Lohse theory, which even yields the approximate magnitude. The corresponding scalings for Re_{OB}^{pl} , Re_m^{pl} , and Re_c^{pl} are given in figure 12(b), showing that here the $1-\sigma$ uncertainty estimates are about 7%.

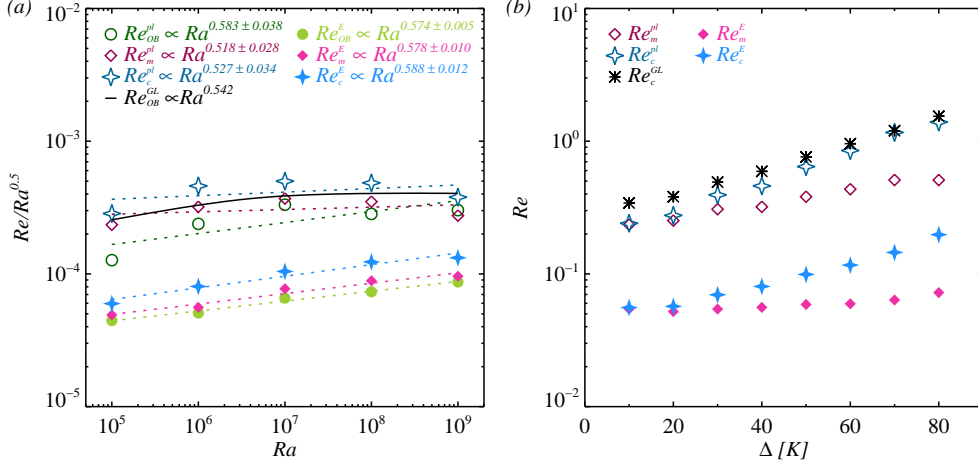


FIGURE 12. (a) Reduced Reynolds number $Re/Ra^{0.5}$ as function of Ra , based on the the maximal plume velocity Re^{pl} and the specific kinetic energy Re^E . Each defined in two ways: with the viscosity at T_m and with that at T_c , denoted by the index m and c , respectively. The dashed line shows the corresponding fitted power laws and the resulting scaling is shown in the legend. The black line shows the effective Grossmann–Lohse scaling for this range under OB conditions. (b) Similar to (a), showing Re^{pl} and Re^E under various NOB conditions as function of Δ for $Ra = 10^6$. The black asterisks show Re based on the Grossmann–Lohse theory evaluated for Pr_c and Ra_c .

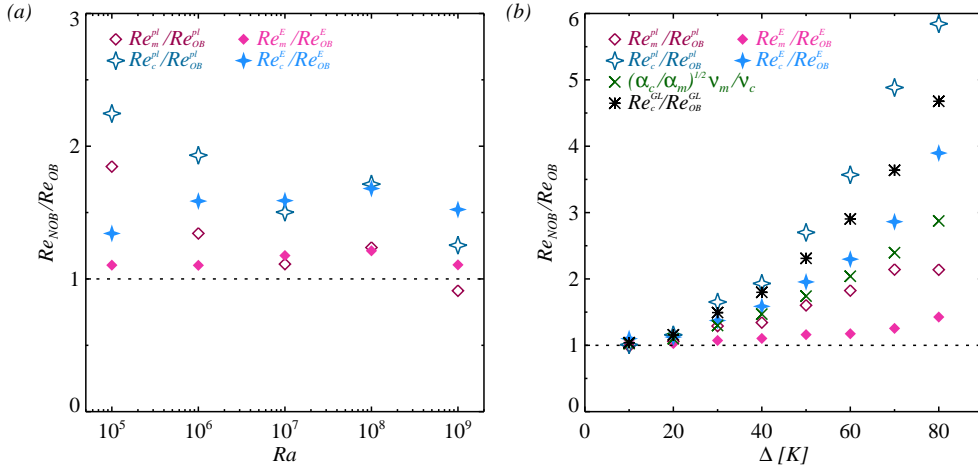


FIGURE 13. Ratio Re_{NOB}/Re_{OB} for the Reynolds numbers as defined in figure 12. The dashed line marks where $Re_{NOB} = Re_{OB}$. (a) Re_{NOB}/Re_{OB} versus Ra for $\Delta = 40$ K (b) Re_{NOB}/Re_{OB} versus Δ for $Ra = 10^6$. The green crosses show the ratio assuming that Re scales with the free-fall velocity, $(\alpha_c/\alpha_m)^{1/2} \nu_m/\nu_c$ as suggested by Sugiyama *et al.* (2009). The black asterisks shows the ratio based on the Grossmann–Lohse theory, evaluated for Pr_c and Ra_c and for their respective values under OB conditions, Pr_m and Ra_m .

Remarkably, the NOB data agree much better, even within the uncertainty, with the Grossmann–Lohse theory than the OB data. We assume that our scaling is significantly influenced by the occurring coherent structures. Other deviations might be caused by the fact that the Grossmann–Lohse theory assumes a single wind amplitude originating

in the LSC, that furthermore needs to be uniform throughout the Rayleigh–Bénard cell, while we have more complex spatial flow structures.

Figure 12(b) presents Re as a function of Δ for constant $Ra = 10^6$. Due to the reduced viscosity ν_c in the bulk, the deviation between the two curves for Re_m and Re_c becomes considerably larger with increasing Δ . By evaluating them for the material properties at T_c , equivalent to using Ra_c and Pr_c , a general agreement of Re_c^{GL} with Re_c^{pl} and the principal dependence on Δ can be obtained, especially for higher Δ .

Figure 13 shows the dependence of the ratios of the NOB to the OB Reynolds numbers on Ra and Δ . For constant $\Delta = 40$ K, see figure 13(a), the data appear just scattered. However, as seen in figure 13(b), for $Ra = 10^6$ and varying Δ , they follow a clear increasing trend. Re_c^{pl} is most sensitive to NOB effects, for $\Delta = 80$ K the Reynolds number is 6 times higher than in the OB case; Re_m^E is least sensitive to NOB effects, being only 1.5 times higher in that case. Assuming that U_{tot}^E is similar to the free-fall velocity $\sqrt{\alpha g \Delta H}$, Sugiyama *et al.* (2009) obtained that the ratio Re_{NOB}^E/Re_{OB}^E should be proportional to $(\alpha_c/\alpha_m)^{1/2} \nu_m/\nu_c$. This is a very rough estimate, being equivalent to a scaling of $Re \propto Ra^{1/2} Pr^{-1/2}$. Nonetheless, the agreement with our obtained DNS data is satisfactory. A refinement of this method would be to use the scaling relations proposed by Grossmann & Lohse (2002). Indeed, this predicts the Δ dependence better, especially for higher Δ .

4.7. Heat transfer and Nusselt number scaling

The dimensionless heat flux, expressed in terms of the Nusselt number Nu , equation (4.4), is another important output parameter. High Prandtl number fluids distinguish themselves by a strong convective heat transfer. With our definition of the BLs in equations (4.2)–(4.3), the Nusselt number in the NOB case is given by the exact relation

$$Nu_{NOB} = \frac{H}{\lambda_t^\theta + \lambda_b^\theta} \frac{\kappa_t \Delta_t + \kappa_b \Delta_b}{\kappa_m \Delta}, \quad (4.30)$$

as was shown by Ahlers *et al.* (2006). This equation looks similar to the well-known equation in the OB case,

$$Nu_{OB} = \frac{H}{2\lambda_{OB}}, \quad (4.31)$$

and a straightforward calculation then yields for the ratio of the NOB to the OB Nusselt number

$$\frac{Nu_{NOB}}{Nu_{OB}} = \frac{2\lambda_{OB}}{\lambda_t + \lambda_b} \frac{\kappa_t \Delta_t + \kappa_b \Delta_b}{\kappa_m \Delta} = F_\lambda F_\Delta. \quad (4.32)$$

The factors F_λ and F_Δ and their product are displayed in figure 14. In the case of glycerol, the heat conductivity Λ , or in our case, equivalently the heat diffusivity κ , depends only very weakly on the temperature. Thus $F_\Delta \simeq 1$ for our considered temperature range. The important factor for the deviation of the Nusselt number rather originates from F_λ and not from F_Δ as in the case of water, this was also found by Sugiyama *et al.* (2007) and was implicitly assumed by Zhang *et al.* (1997). Since we are neither steady nor turbulent, but always plume-dominated or transitional, the Nusselt number depends in a strongly non-linear way on Δ and Ra due to the complex and distinct flow patterns. In the two-dimensional simulations by Sugiyama *et al.* (2007), this non-linear behaviour of Nu with Δ was found as well. But evidently, the flow patterns are different under these circumstances. For all our considered combinations of Rayleigh numbers Ra and temperature differences Δ , the deviations are more pronounced in the three-dimensional case.

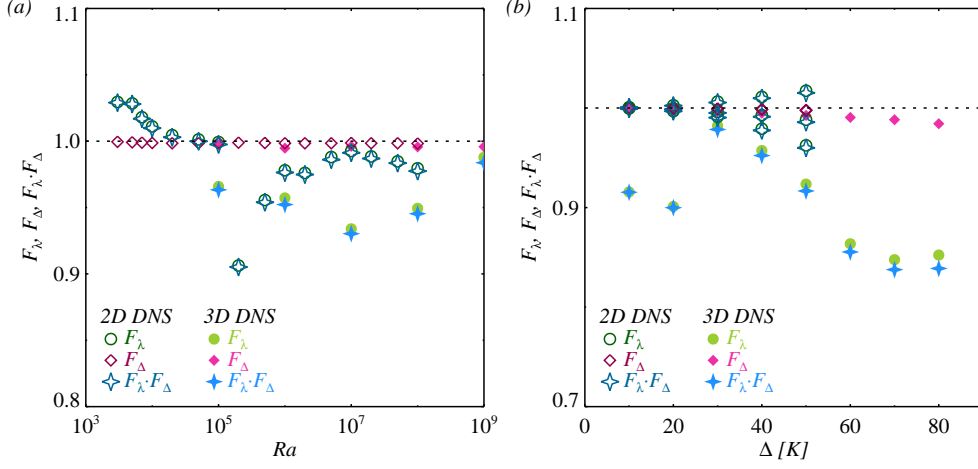


FIGURE 14. Nusselt number ratio $Nu_{NOB}/Nu_{OB} = F_\lambda F_\Delta$ and its contributing factors F_λ and F_Δ . Shown are our 3D DNS data as well as the 2D data from Sugiyama *et al.* (2007). (a) $F_\lambda \cdot F_\Delta$, F_λ and F_Δ versus Ra for $\Delta = 40$ K. (b) $F_\lambda F_\Delta$, F_λ and F_Δ versus Δ for $Ra = 10^6$. The dashed line corresponds to $F = 1$.

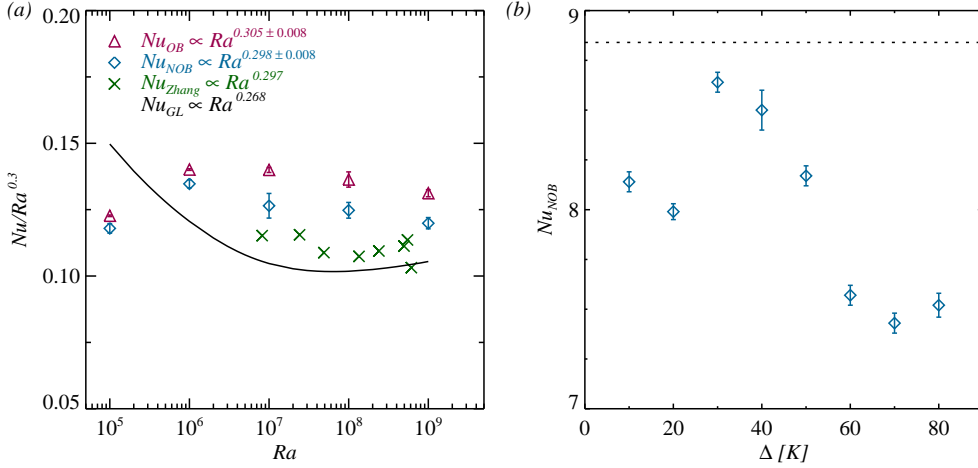


FIGURE 15. (a) Reduced Nusselt number $Nu/Ra^{0.3}$ as a function of Ra under OB (purple triangles) and NOB conditions with $\Delta = 40$ K (blue diamonds). The Nusselt number is evaluated as a plane average, i.e., the vertical heat flux, and the errorbar indicates the standard deviation of the constant Nu profile along z . The experimental data from Zhang *et al.* (1997) (green crosses) are also shown, however, we would like to point out that first, Pr varied between approximately 600 and 8000, second, their Nusselt number is based on a constant κ , i.e., $Nu = H/(\lambda_t^\theta + \lambda_b^\theta)$. The black line shows the effective scaling for the OB case, according to the Grossmann–Lohse theory, equations (4.27)–(4.28). (b) Nu as a function of Δ under NOB conditions for constant $Ra = 10^6$ and varying Δ . The dashed line indicates the OB value.

Figure 15(a) we finally also presents Nu as a function of Ra under OB and NOB conditions, including the scaling predicted by Grossmann & Lohse (2000, 2001) and the experimental data by Zhang *et al.* (1997). The effective exponents can be found in the legend. While the scaling practically does not change under NOB conditions, and the agreement with the experiments is remarkably good considering the different Prandtl

numbers, the Grossmann–Lohse theory slightly underestimates the Nusselt number. The reason might be that the available experimental data to fix the constants in this regime are rather sparse, making scaling predictions less accurate.

5. Concluding remarks

Compared to the plethora of available data for low Prandtl number fluids, the data for high Prandtl number fluids are still rather sparse. To improve our understanding of Rayleigh–Bénard convection, especially with regard to a comprehensive theory, more experiments and numerical simulations in the regime of high Prandtl numbers are not only desirable but also necessary. In the present paper, Rayleigh–Bénard convection of glycerol with $Pr = 2547.9$ was investigated in a cylindrical cell of aspect ratio unity. We focused our attention on the influence of NOB effects, since under ambient conditions the validity range of the OB approximation is severely violated for glycerol. For that purpose, we advanced our OB code (Shishkina & Wagner 2005) by implementing temperature-dependent material properties. We performed three-dimensional DNS in a range of $10^5 \leq Ra \leq 10^9$ for OB conditions and NOB conditions between $10 \text{ K} \leq \Delta \leq 80 \text{ K}$, resulting in a total of 17 different simulation setups. We compared our results to what is, as far as we know, the only available experimental data by Zhang *et al.* (1997, 1998), and numerical (but only two-dimensional) data of Sugiyama *et al.* (2007).

The developing flow patterns in glycerol for lower Ra resemble the behaviour of lower Pr and higher Γ , i.e., we observe several cells. The number of cells, moreover, depends on the imposed Δ . However, for large enough Rayleigh numbers, i.e., $Ra \gtrsim 10^8$, we find a typical LSC as in $\Gamma = 1$ and $Pr = O(1)$ Rayleigh–Bénard convection. This behaviour could not be reproduced in two-dimensional simulations. While these simulations are useful to investigate qualitatively the properties of the three-dimensional flow, three-dimensional DNS are evidently necessary to resolve its full topology.

Under NOB conditions, the perfect symmetry with respect to the horizontal midplane is broken. One of the most remarkable features then is the higher centre temperature. The deviation $T_c - T_m$ is as large as 15 K for $\Delta = 80 \text{ K}$. The obtained T_c s agree perfectly well with the experiments, when only the experimental points for $Pr > 1200$ are considered. For lower Pr , the experimentally obtained centre temperatures are lower. The two-dimensional simulations by Sugiyama *et al.* (2007) yielded a lower T_c than our three-dimensional ones, even though the same Pr was considered in their case. We also compared our results with the predictions of the theoretical and empirical models by Wu & Libchaber (1991); Zhang *et al.* (1997); Manga & Weeraratne (1999), and Ahlers *et al.* (2006). While the 2D boundary layer models by Zhang *et al.* (1997) and Ahlers *et al.* (2006) overestimate the actual T_c , due to the plume emission all over the plate and the not always existing LSC, the models by Wu & Libchaber (1991), based on the same temperature or velocity scales in the boundary layers, predict T_c very well with a standard deviation of 0.4 K.

Furthermore, we analysed the temperature and velocity profiles. Due to the strongly varying viscosity and heat conductivity close to the heating and cooling plates, the temperature profiles bend towards the plate near the cold top plate and farther away from it near the hot bottom plate, whereas the situation for the velocity profiles is the other way round: they bend farther away from the top plate and closer to the bottom plate. This also induces different thermal and viscous boundary layer thicknesses. The top boundary layers are always thicker than the bottom ones. Their ratio is up to 2.5 for the thermal and up to 4.5 for the viscous boundary layers.

The two important output parameters of Rayleigh–Bénard convection, the Reynolds

number Re and the Nusselt number Nu , were investigated as well. In the parameter range considered, Re is always higher and Nu is always lower under NOB than under OB conditions. We evaluated Re for different choices of the characteristic velocity, i.e., based on the total volume averaged kinetic energy U_{tot}^E and the plume velocity U^{pl} , and for different choices of the characteristic viscosity, i.e., the mean and the centre viscosity ν_m and ν_c . The absolute value of Re is highly sensitive, but the scaling with Ra is only slightly sensitive, to the choice of the characteristic scales. For $Ra = 10^6$ and $\Delta = 80$ K, the Reynolds number defined with U^{pl} and ν_c is up to 6 times higher than in the OB case. This increase can be described with satisfactory accuracy by the Grossmann–Lohse theory based on Ra_c and Pr_c . The Nusselt number Nu is influenced in a non-linear way by NOB effects, and more strongly than was suggested by the two-dimensional simulations.

The scaling of Nu with Ra shows no significant difference between NOB and OB conditions, i.e., $Nu_{OB} \propto Ra^{0.305}$ and $Nu_{NOB} \propto Ra^{0.298}$. The NOB scaling is in excellent agreement with the experimental data.

The authors acknowledge support by the *Deutsche Forschungsgemeinschaft (DFG)* under grant SH405/2-1. Furthermore, the authors would like to thank the *Leibniz-Rechenzentrum (LRZ)* in Garching for providing computational resources on the national supercomputer HLRB-II under grant pr47he.

REFERENCES

- AHLERS, G., BROWN, E., FONTENELE ARAUJO, F., FUNFSCHILLING, D., GROSSMANN, S. & LOHSE, D. 2006 Non-Oberbeck-Boussinesq effects in strongly turbulent Rayleigh–Bénard convection. *J. Fluid Mech.* **569**, 409–445.
- AHLERS, G., FONTENELE ARAUJO, F., FUNFSCHILLING, D., GROSSMANN, S. & LOHSE, D. 2007 Non-Oberbeck-Boussinesq Effects in Gaseous Rayleigh–Bénard Convection. *Phys. Rev. Lett.* **98**, 054501.
- AHLERS, GUENTER, GROSSMANN, SIEGFRIED & LOHSE, DETLEF 2009 Heat transfer and large scale dynamics in turbulent rayleigh–bénard convection. *Reviews of Modern Physics* **81** (2), 503.
- BOUSSINESQ, J. 1903 *Théorie analytique de la chaleur*. Gauthier-Villars Paris.
- BREUER, M., WESSLING, S., SCHMALZL, J. & HANSEN, U. 2004 Effect of inertia in Rayleigh–Bénard convection. *Phys. Rev. E* **69** (2), 26302.
- BURNISHEV, Y., SEGRE, E. & STEINBERG, V. 2010 Strong symmetrical non-Oberbeck–Boussinesq turbulent convection and the role of compressibility. *Phys. Fluids* **22** (3), 035108.
- BUSSE, F. H. 1967 The stability of finite amplitude cellular convection and its relation to an extremum principle. *J. Fluid Mech.* **30**, 625–649.
- BUSSE, F. H. 1978 Non-linear properties of thermal convection. *Rep. Prog. Phys.* **41**, 1929–1967.
- BUSSE, F. H. 1979 High Prandtl number convection. *Phys. Earth Planet. Inter.* **19**, 149–157.
- CASTAING, B., GUNARATNE, G., KADANOFF, L., LIBCHABER, A. & HESLOT, F. 1989 Scaling of hard thermal turbulence in rayleigh–bénard convection. *J. Fluid Mech.* **204**, 1–30.
- CHRISTENSEN, U. & HARDER, H. 1991 3-D convection with variable viscosity. *Geophys. J. Int.* **104**, 213–226.
- CONSTANTIN, P. & DOERING, C. R. 1999 Infinite Prandtl Number Convection. *J. of Stat. Phys.* **94** (1/2), 159–172.
- GETLING, A. V. 1998 *Rayleigh–Bénard convection: structures and dynamics*. World Scientific Publishing Co. Pte. Ltd.
- GRAY, D. D. & GIORGINI, A. 1976 The validity of the Boussinesq approximation for liquids and gases. *Int. J. Heat Mass Transfer* **19**, 545–551.
- GROSSMANN, S. & LOHSE, D. 2000 Scaling in thermal convection: A unifying theory. *J. Fluid Mech.* **407**, 27–56.

- GROSSMANN, S. & LOHSE, D. 2001 Thermal convection for large Prandtl numbers. *Phys. Rev. Lett.* **86** (15), 3316–3319.
- GROSSMANN, S. & LOHSE, D. 2002 Prandtl and Rayleigh number dependence of the Reynolds number in turbulent thermal convection. *Phys. Rev. E* **66** (1), 16305.
- HORN, S., SHISHKINA, O. & WAGNER, C. 2011 The influence of non-Oberbeck–Boussinesq effects on rotating turbulent Rayleigh–Bénard convection. *J. Phys.: Conf. Ser.* **318**, 082005.
- KRISHNAMURTI, R. & HOWARD, L. N. 1981 Large-scale flow generation in turbulent convection. *Proc. Natl. Acad. Sci. USA* **78** (4).
- MANGA, M. & WEERARATNE, D. 1999 Experimental study of non-Boussinesq Rayleigh–Bénard convection at high Rayleigh and Prandtl numbers. *Phys. Fluids* **11** (10), 2969–2976.
- OBERBECK, A. 1879 Ueber die Wärmeleitung der Flüssigkeiten bei Berücksichtigung der Strömungen infolge von Temperaturdifferenzen. *Annalen der Physik* **243** (6), 271–292.
- OGAWA, M., SCHUBERT, G. & ZEBIB, A. 1991 Numerical simulations of three-dimensional thermal convection in a fluid with strongly temperature-dependent viscosity. *J. Fluid Mech.* **233**, 299–328.
- SCHMALZL, J., BREUER, M. & HANSEN, U. 2004 On the validity of two-dimensional numerical approaches to time-dependent thermal convection. *Europhys. Lett.* **67** (3), 390–396.
- SCHMITT, L. & FRIEDRICH, R. 1988 Large-eddy simulation of turbulent backward facing step flow. In *7th GAMM-Conference on Numerical Methods in Fluid Mechanics*, pp. 355–362. Vieweg und Sohn.
- SCHUMANN, U. 1975 Subgrid scale model for finite difference simulations of turbulent flows in plane channels and annuli. *J. Comput. Phys.* **18** (4), 376–404.
- SEGUR, J. B. & OBERSTAR, H. E. 1951 Viscosity of glycerol and its aqueous solutions. *Ind. Eng. Chem.* **43**, 2117–2120.
- SHISHKINA, O., STEVENS, R. J. A. M., GROSSMANN, S. & LOHSE, D. 2010 Boundary layer structure in turbulent thermal convection and its consequences for the required numerical resolution. *New J. Physics* **12**, 075022.
- SHISHKINA, O. & WAGNER, C. 2005 A fourth order accurate finite volume scheme for numerical simulations of turbulent Rayleigh–Bénard convection in cylindrical containers. *C. R. Mecanique* **333**, 17–28.
- SHISHKINA, O. & WAGNER, C. 2006 Analysis of thermal dissipation rates in turbulent Rayleigh–Bénard convection. *J. Fluid Mech.* **546**, 51–60.
- SHISHKINA, O. & WAGNER, C. 2007a Boundary and interior layers in turbulent thermal convection in cylindrical containers. *Int. J. Computing Science and Mathematics* **1**, 360–373.
- SHISHKINA, O. & WAGNER, C. 2007b A fourth order finite volume scheme for turbulent flow simulations in cylindrical domains. *Computers & Fluids* **36**, 484–497.
- SILANO, G., SREENIVASAN, K. & VERZICCO, R. 2010 Numerical simulations of Rayleigh–Bénard convection for Prandtl numbers between 10^{-1} and 10^4 and Rayleigh numbers between 10^5 and 10^9 . *J. Fluid Mech.* **662**, 409–446.
- STEVENS, R. J. A. M., VERZICCO, R. & LOHSE, D. 2010 Radial boundary layer structure and Nusselt number in Rayleigh–Bénard convection. *J. Fluid Mech.* **643**, 495–507.
- SUGIYAMA, K., CALZAVARINI, E., GROSSMANN, S. & LOHSE, D. 2007 Non-Oberbeck–Boussinesq effects in two-dimensional Rayleigh–Bénard convection in glycerol. *Europhys. Lett.* **80**, 34002.
- SUGIYAMA, K., CALZAVARINI, E., GROSSMANN, S. & LOHSE, D. 2009 Flow organization in two-dimensional non-Oberbeck–Boussinesq effect Rayleigh–Bénard convection in water. *J. Fluid Mech.* **637**, 105–135.
- WAGNER, S., SHISHKINA, O. & WAGNER, C. 2012 Boundary layers and wind in cylindrical Rayleigh–Bénard cells. *J. Fluid Mech.* **697**, 336–363.
- WU, X. Z. & LIBCHABER, A. 1991 Non-Boussinesq effects in free thermal convection. *Phys. Rev. A* **43** (6), 2833–2839.
- XIA, KE-QING, LAM, SIU & ZHOU, SHENG-QI 2002 Heat-flux measurement in high-prandtl-number turbulent rayleigh–bénard convection. *Phys. Rev. Lett.* **88**, 064501.
- ZHANG, J., CHILDRESS, S. & LIBCHABER, A. 1997 Non-Boussinesq effect: Thermal convection with broken symmetry. *Phys. Fluids* **9** (4), 1034–1042.
- ZHANG, J., CHILDRESS, S. & LIBCHABER, A. 1998 Non-Boussinesq effect: Asymmetric velocity profiles in thermal convection. *Phys. Fluids* **10**, 1534.